Università degli Studi di Genova

Scuola di Scienze Matematiche, Fisiche e Naturali, Dipartimento di Fisica

Ph.D Thesis in Physics

XXX Cycle, Academic Years 2014-2017

"The Anticoincidence Detector onboard the Athena X-Ray observatory"

Dario Corsini

Supervisor: Flavio Gatti

Contents

Introduction

X-Rays in the energy range of hundreds of eV can penetrate the interstellar gas over distances comparable to the size of our galaxy, without being completely absorbed, depending on the direction of the line of sight. At higher energies, however, they can penetrate the gas medium too, reaching distances comparable to the radius of the Universe. Also, they can be easily focused by special telescopes, distinguishing them from Gamma-Rays.

They reveal the existence of astrophysical processes in which matter has been heated up to temperatures of millions of degrees, or in which particles have been accelerated to relativistic energies: that is, processes in which the total energy is extremely high, such in Supernova explosions, or Active Galactic Nuclei emissions, or events in which the energy acquired per nucleon or the temperature of the matter involved is extremely high, like infall onto collapsed objects, high-temperature plasmas, interaction of relativistic electrons with magnetic or photon fields.

For all these reasons, studying X-Rays of astronomical origin has been a key question since the discover of the first X-Ray source in the late 60s by Giacconi et al, Sco-X1 [1].

What it has been more and more clear since then, is that the Universe is dominated by high energy processes, and exploring it through the window of X-Rays could allow us to uncover its secrets.

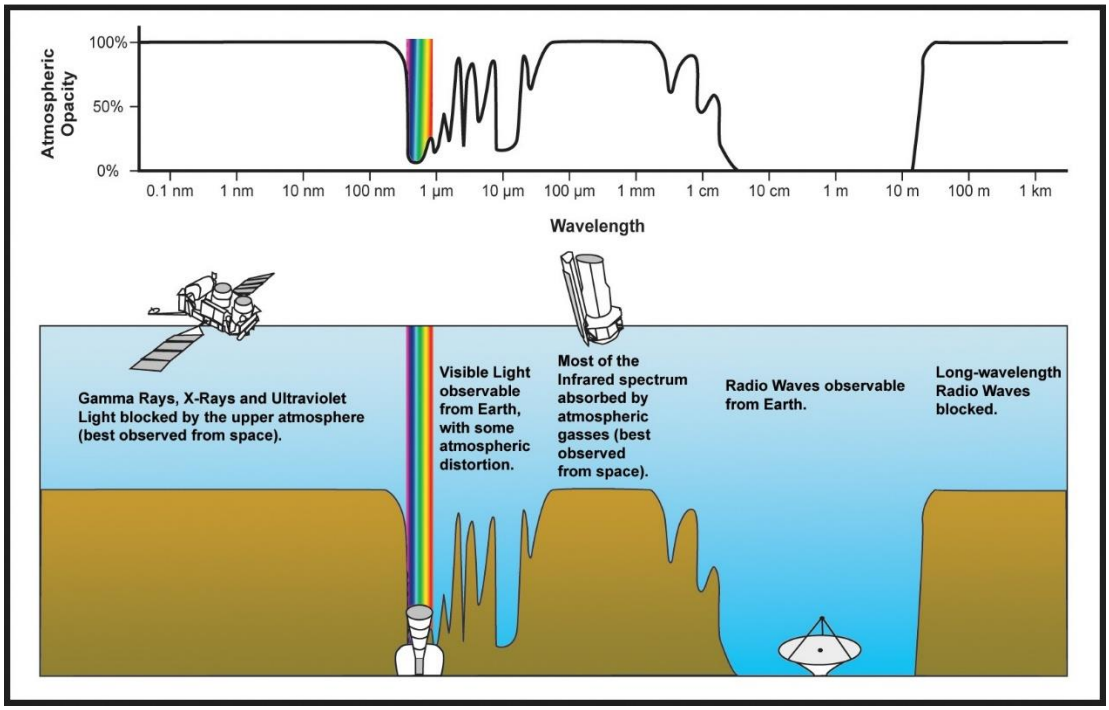

Figure I: Atmosphere opacity over a wide wavelength spectrum.

As we can observe in Figure I, X-Rays would never be observable from ground-based experiments, since our atmosphere is completely opaque at their wavelength.

This is the reason why over the past years, rockets and satellites have been developed in order to study this branch of Astrophysics.

First experiments were carried out by rockets with proportional counters: photons ionize a small volume of gas, producing a signal proportional to the number of events. This was the case of the mission AS&E, first, and UHURU, later, whose sensitivity was increased by a factor 10^4, using a larger detection area. Problems linked to this kind of the detectors were mainly due to the scalability: further improvements would require very large areas, impossible to carry onto a rocket. To overcome this problem, focussing mirrors for X-Rays were developed, allowing to manufacture smaller detectors, while increasing the angular resolution. Of course, the use of rockets was not possible anymore. Telescopes for X-Ray Astrophysics were born, with the first being the Einstein telescope [2].

Technology did not stop: beside the development of focussing mirrors, also detectors changed their face. Solid State Detectors (SSDs) are more sensitive and can be assembled in very small arrays, so to reconstruct an accurate image of an X-Ray source. Chandra observatory, which is still flying and getting marvellous images of our X-Ray Universe, uses a 1024 x 1024 pixels array (ACIS [3]).

Now, more powerful detectors and even more efficient mirrors are being developed, for the next generation of X-Ray telescopes.

Figure II plots a graphic of the changes occurred in 40 years of X-Ray observations: it is astonishing to observe the huge leap in the sensitivity for even extremely low fluxes.

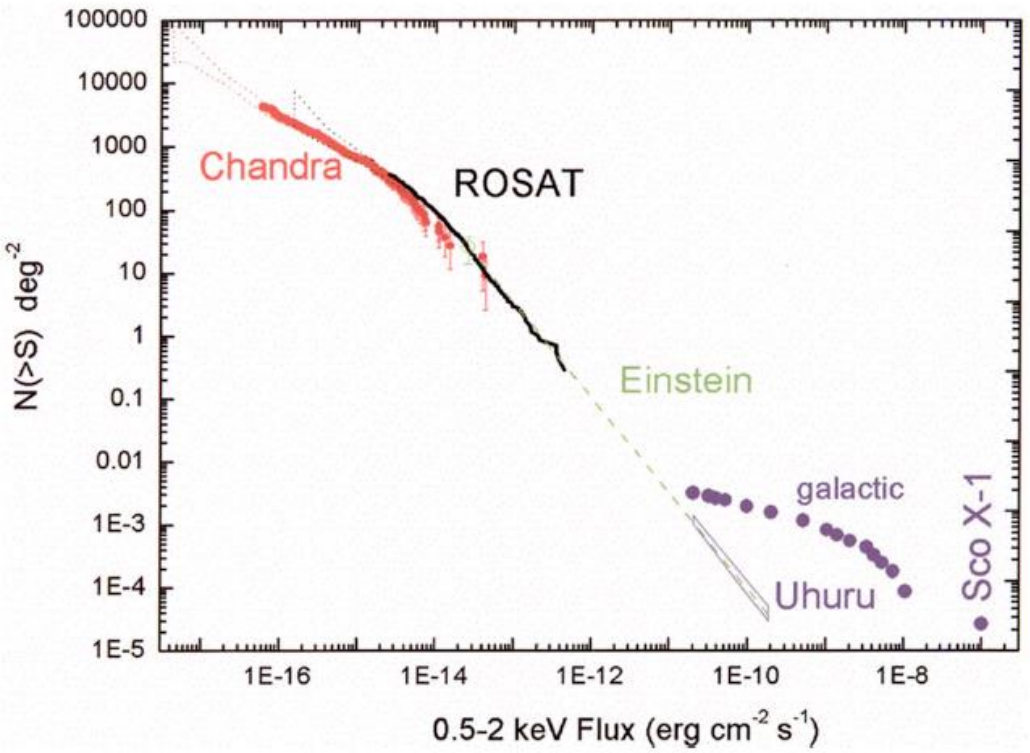

Figure II: Sensitivity change from 1962 (SCO X-1) to 2000 (Chandra). [4]

As we are developing more and more powerful technology to probe this field, more interesting phenomena and new physics, which we could not see before, is

found. Also, by discovering large-scale processes in our Universe, we have become aware that it is not just a quiet place dominated by the consumption of nuclear fuel, but a place where high energy, catastrophic phenomena and enormous explosions take place every second, shaping it and leading its evolution, from the initial explosion to the formation of galaxies and clusters, from the birth to the death of stars.

Chandra and XMM Newton have been flown for more than a decade, and their technology has already been pushed to the limit.

Meanwhile, new technologies have been developed, allowing to jump towards the next generation of X-Ray telescopes.

In particular, starting from the new millennium, there have been efforts in developing detectors based on superconducting sensors. The technology required for such observatory proposed, namely Xeus, then IXO, was not yet mature. As this second decade is approaching, the research has finally reached a level of readiness suitable to put together every piece and create a satellite able to dig the deepest secrets of our Universe, and to outreach the previous capability on field.

It has been a long way, and there’s still plenty of road ahead, but since 2015, the path has been tracked: ATHENA is going to be the observatory every Astronomer was waiting for.

1. The ATHENA Mission

The X-Ray observatory ATHENA (Advanced Telescope for High ENergy Astrophysics) has been selected for the science theme “The Hot and Energetic Universe” for the ESA Cosmic Vision 2015-2025. [5]

Its purpose is to answer some important questions in Astrophysics in the X-Ray band (0.02 - 12 keV). Among all, two of the main themes are the following [6]:

- How does ordinary matter stick together in the large–scale structure known as the Cosmic Web;
- What’s the role of supermassive Black Holes in shaping the Universe, the so called Cosmic Feedback.

These two themes need to be studied in different ways, but both are explored the best through the analysis of X-Ray emissions, since the first keeps tracks of the baryonic component of the Universe, bound together in a hot gas at the temperature of 10^6 K, while the latter needs to take into account extreme energetic processes occurring at the event horizon of Black Holes.

There are many other topics which can be studied by ATHENA, due to its capabilities: understanding the structure and energetics of stellar winds and their interplay with planets’ atmospheres and magnetospheres; exploring the behaviour of matter under extreme conditions of density and magnetic fields in neutron stars; probe the elements and the physics of heating the Inter–Stellar Medium by supernova explosions.

ATHENA is a leap forward in space based, High Energy Astrophysics experiments. To guarantee the science goal are fulfilled, the best technology is required.

1.1. The Cosmic Web: Missing Hot Baryons and WHIM

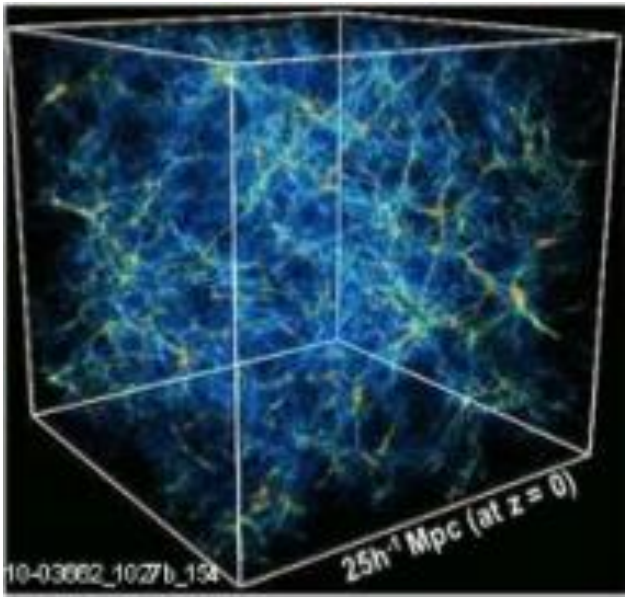

Figure 1.1: Hydrodynamic simulation of the Cosmic Web on high scale.

Figure 1.1 shows an interesting simulation concerning the so called Cosmic Web, on a cubic large portion of Universe, with an edge of roughly 40 Mpc (around 10^{18} m).

Our current Cosmological Model foresees a Baryonic abundance of about the 5% of the mass-energy budget of the Universe, while Dark Matter and Dark Energy complete the rest. Despite this low percentage, still a high amount of baryons are not detected (~30%).

It is supposed that this missing amount can be found in a hot, rarefied state, connecting clusters in a web; a Cosmic Web, which is therefore called Warm Hot Intergalactic Medium (WHIM). Simulations like that shown in Figure 1.1 assess that baryons can be found into these long, low-density filaments of gas at temperature ~10^6 K. Due to the low-density characteristic and the gas temperature, its continuum emission is very faint and dominated by background. H and He are completely ionized, so the only way to characterize the WHIM is the direct observation of highly ionized metals (C, N, O, Ne, Fe) [7].

This is why a high energy resolution and capability to perform spectroscopy of extended sources are needed.

An example of ATHENA spectral capabilities is shown in Figure 1.2.

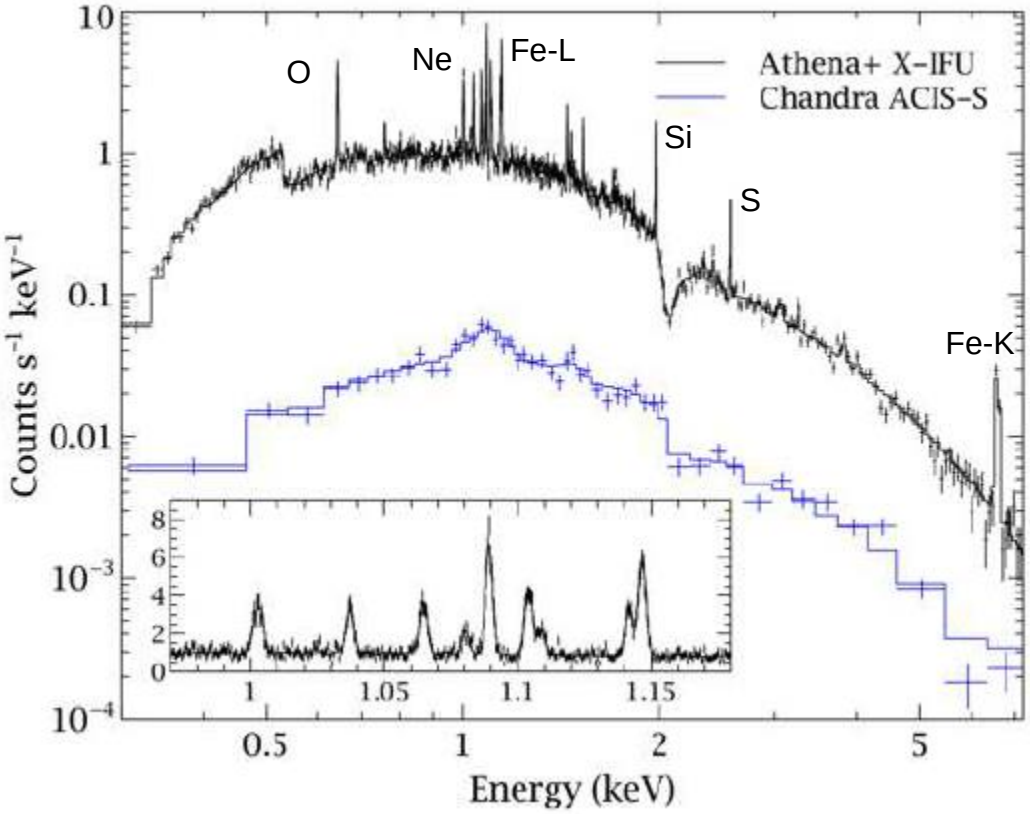

Figure 1.2: Simulated ATHENA observations of the Perseus cluster, highlighting the advanced capabilities for revealing the intricacies of the physical mechanisms at play. The spectrum is a single 5" x 5" region of the cluster, with the existing Chandra ACIS spectrum for comparison. The inset shows the region around the Fe-L complex. Moreover, such measurements will allow us to pinpoint the locations of jet energy dissipation, determine the total energy stored in bulk motions and weak shocks, and test models of AGN fuelling so as to determine how feedback regulates hot gas cooling [8].

ATHENA will be able to reconstruct a 3D map through redshifts measurements of the same lines.

1.2. Supermassive Black Holes and Cosmic Feedback

Some galaxies have a compact nucleus that outshines the light of stars inside them: they can only be explained by stellar emission models with the implementation of accreting supermassive black holes (SMBH): we refer to them as Active Galactic Nuclei (AGN). The ubiquity of supermassive black holes (SMBH) in local galaxy spheroids has been established [9], and we suspect that a strong correlation between the presence of a SMBH inside a galaxy and its accretion exists [10].

What we do not know is the nature of this link, and we need further investigations.

Matter falling into a black hole, due to the dynamical friction, causes the emission of a strong signal in the X-Ray band. For this reason, using X-Ray facilities is a well suitable instrument to probe for this physic.

The best window to look for the interaction of SMBH and their hosting galaxies lies at z~1÷4, when most black holes and stars we see in the present-day Universe were put in place. Unfortunately, our efforts to probe this field could only be limited to the local Universe [11].

This limit is due to the large amount of gas and dust in these high z galaxies, which are still giving birth to new stars. AGN inside them are obscured since the gas/dust density is exceeding the Thomson scattering cross-section. These sources are called Compton thick AGN. As a consequence, these important sources are extremely faint and actual missions are not able to fully characterize them.

To characterize a Compton thick AGN it is useful to highlight the presence of a strong K_α Iron emission line, and to fully analyse the X-Ray continuum as absorption spectrum. Figure 1.3 shows the performances expected for Athena, with respect to an actual observation of Chandra.

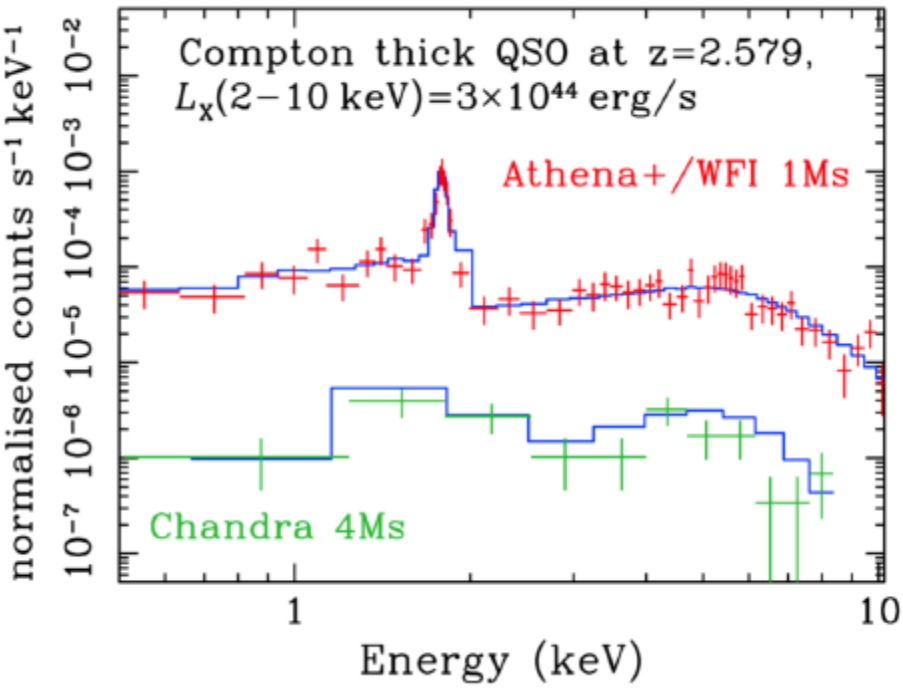

Figure 1.3: Heavily obscured AGN at z=2.579. Red points are simulated for Athena Wide Field Imager instrument for a 1 Ms survey, with the K_α line well visible. Green points refer to a 4 Ms Chandra Deep Field South real observation.

1.3. The ATHENA Observatory

The payload consists of an X-Ray telescope, with a Silicon Pore Optics focusing technology, and two focal plane instruments: The Wide Field Imager (WFI), a camera for high field of view, based on Depleted P Field–Effect Transistors (DePFET), and an X-Ray Integral Field Unit (X-IFU), a cryogenic spectrometer based on a large array (more than 3000) of Transition-Edge Sensor (TES) microcalorimeters, with a 5' field of view, an angular resolution of 5", and a very high energy resolution of 2.5 eV at 6 keV.

This is the same technology flown on-board the Hitomi Astro-H satellite [12], who made use of a smaller TES array (6x6) and a lower observation orbit. Before the mission ended unexpectedly, it was able to provide very impressive results on the potential of TES technology applied to X-Ray Astrophysics [13] [14].

Launch readiness is planned for 2028, by means of an Ariane V or VI rocket. Unlike Astro-H, ATHENA will operate at L2 (second Lagrangian point of the Sun-Earth system), since it provides a very stable thermal environment and good observing performances.

ATHENA will predominantly perform pointed observations, with durations ranging from 10^3 to 10^6 seconds. There will also be the possibility for opportunity targets observations, such for gamma ray burst or other transient-like events.

1.3.1. Spacecraft and Optics

Previous studies have addressed many characteristics and requirements needed for ATHENA. Major heritages also come from XMM-Newton. The spacecraft will be composed of three main parts:

- The service module;
- The mirror assembly module;
- The focal plane module;

The service module consists of a fixed metering structure between the mirror and the focal plane modules, which should give a focal length of 12 meters. It is optimized to have a low momentum of inertia for fast repointing purposes. It accommodates standard functions, including attitude and orbit control system, propulsion, thermal, telemetry and telecommanding, power and data handling subsystems. It will also mount the solar panels required to power the satellite.

The mirror assembly module employs Silicon Pore Optics (SPO) to reflect X-Rays to the focal plane module. It is a highly modular concept, based on a set of compact individual mirror modules: an innovative technology that has been pioneering in Europe over the last decades. Together with the focal length provided by the service module, it helps reach an effective area of 2 m^2 at 1 keV [15].

The focal plane module hosts the two measuring instruments: the Wide Field Imager (WFI) and the X-Ray Integral Field Unit (X-IFU), inside a dedicated cryostat.

Figure 1.4 shows a representation of the ATHENA spacecraft, where the three modules can be seen. Figure 1.5 shows the details concerning the mirror assembly module.

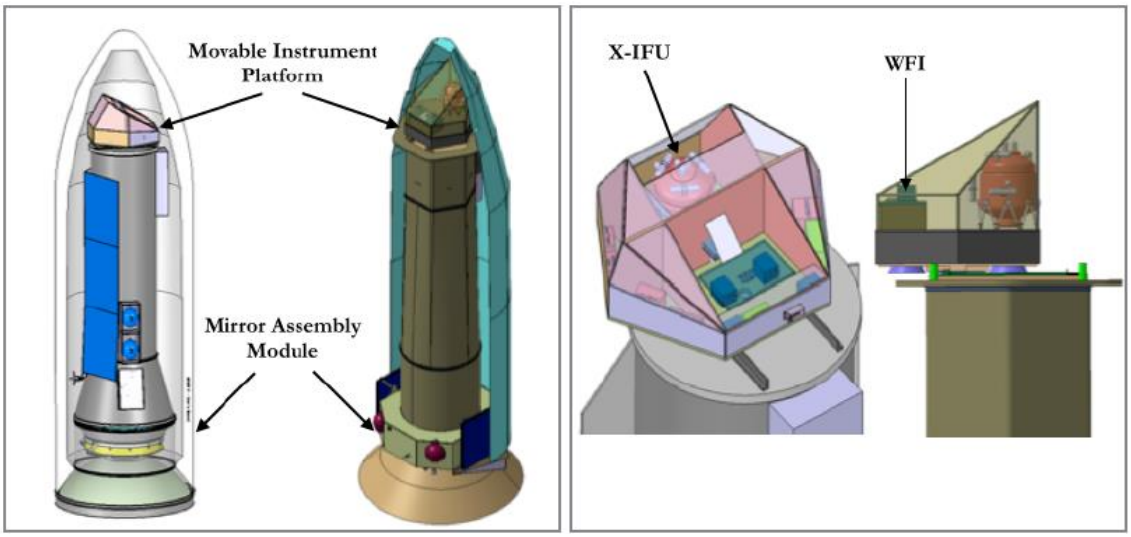

Figure 1.4: (LEFT) Spacecraft configuration during launch from Thales-Alenia-Space (TAS, left) and Airbus Defence & Space (ADS, right). (RIGHT) MIP configurations from TAS (left) and ADS (right).

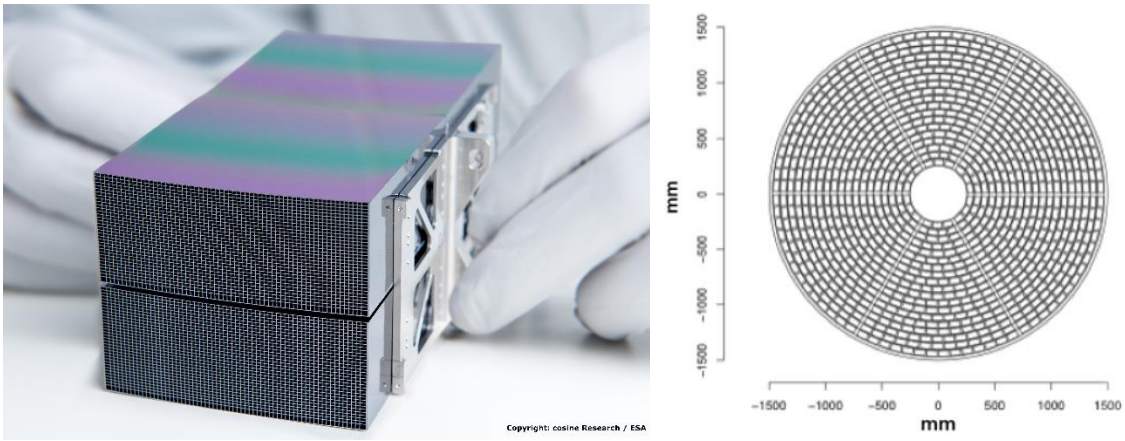

Figure 1.5: (LEFT) a complete SPO module pack. (RIGHT) configuration of the mirror assembly module, with 972 SPO modules arranged in 6 sectors and 19 rings.

1.3.2. The Wide Field Imager (WFI)

The Wide Field Imager (WFI) [16], is one of the two instruments composing the focal plane of ATHENA. It brings together a large field of view of 40’ x 40’, with an excellent count rate capability, higher than 1 Crab.

It is made by silicon active pixel sensors of DEPFET (depleted p-channel field effect transistors), with a resolution FWHM less than 170 eV @ 7 keV, in the range 0.2 to 15 keV energy bandwidth.

Two detectors are planned: a large 1024 x 1024 pixels array and a smaller, fast detector, optimized for high count-rate observations.

WFI is also composed by many other parts: filter wheels with optical stray-light baffle, camera head comprising the detectors and their electronics, all mounted on a primary structure, accommodated on the focal plane module (FPM). The instrument control and power distribution units (ICPUs) are also found in the same module, together with the radiation panels.

Figure 1.6 shows the block diagram for WFI, and Table 1.1 summarizes its main parameters and requirements.

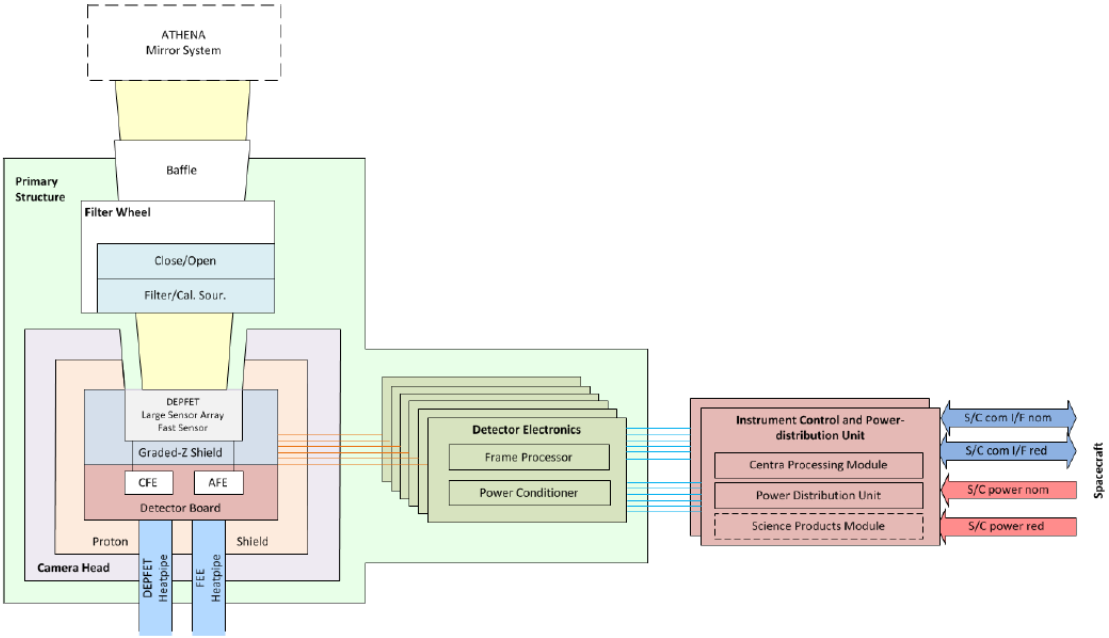

Figure 1.6: Block diagram for the FWI, showing the components of the instrument.

Parameter	***Value***
Energy range	*0.2 – 15 keV*
Pixel Size	*130 µm x 130 µm (2.2 arcsec x 2.2 arcsec)*
Operating Mode	*Rolling shutter (min. power consumption)* *full frame mode* *optional: window mode*
High-count rate detector	*64 x 64 pixels, mounted defocussed* *split full frame readout time resolution: 80 µs* *1 Crab > 90% throughput and < 1% pile-up*
Large-area DEPFET	*4 quadrants, each with 512 x 512 pixels (total FOV 40' x 4o')* *Time resolution: < 5 ms*
Quantum efficiency *including external filters*	*> 20% @ 277 eV* *> 80% @ 1 keV* *> 90% @ 10 keV* *Transmissivity for optical photons: 3 x 10^{-7}* *Transmissivity for UV photons: < 10^{-9}*
Energy resolution	*FWHM (7 keV) < 170 eV*
Non X-Ray background	*< 5 x 10^{-3} cts/cm^2/s/keV*

Table 1.1: WFI main parameters.

1.3.3. The X-Ray Integral Field Unit (X-IFU)

The high spectral resolution instrument on-board ATHENA will be represented by the X-Ray Integral Field Unit, or X-IFU [17], a spectrometer based on an array of about 3800 Transition-Edge Sensors microcalorimeters, working at a base temperature of 50 mK, a field of view of 5' with an angular resolution of 5", and an outstanding energy resolution of 2.5 eV at 6 keV.

Its characteristics allow it to reach the goals of the Hot and Energetic Universe scientific theme, being able to spatially and energetically resolve the presence of baryons in hot gases.

As for the WFI, X-IFU is composed by many other components: the 2 K stage focal plane assembly (FPA) hosts the 50 mK stage with the TES array as well as the cryogenic anticoincidence detector, the cold front-end electronics (CFEE) and the filter wheels (FW). Other stages host the warm front-end electronics (WFEE) with the digital readout electronics (DRE) and many more, as it can be seen in Figure 1.7.

Table 1.2 reports X-IFU main requirements, based on the scientific themes to fulfil.

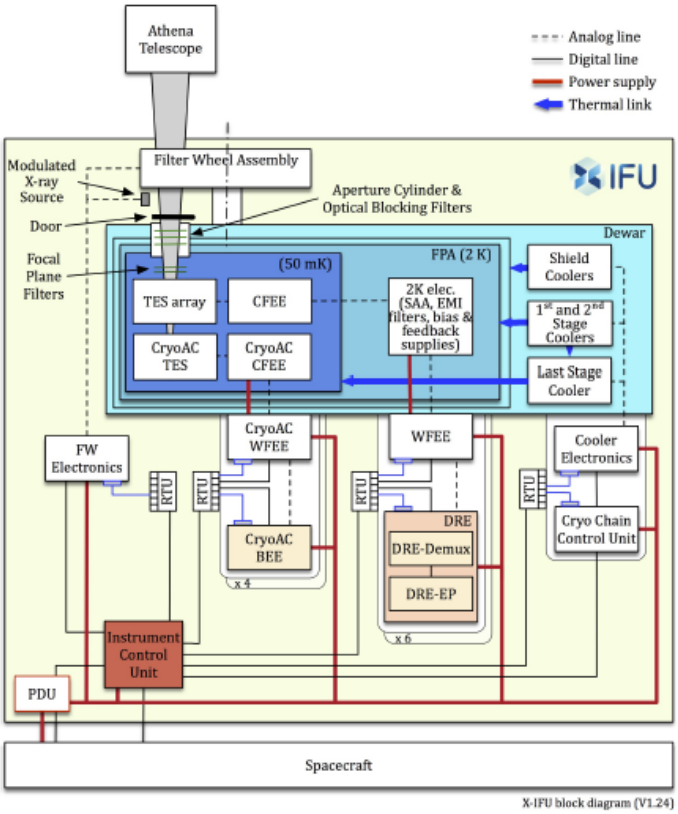

Figure 1.7: X-IFU block diagram. The main TES array together with the cryogenic anticoincidence CryoAC TES are the sensing parts of the instrument, which is composed of many other components.

Parameter	***Value***
Energy range	*0.2 – 12 keV*
Energy resolution < 7 keV	*2.5 eV*
Energy resolution > 7 keV	*E/ΔE = 2800*
Field of View	*5 arcmin*
Effective Area @ 0.3 keV	*> 1500 cm^2*
Effective Area @ 1 keV	*> 15000 cm^2*
Effective Area @ 7 keV	*> 1600 cm^2*
Gain Calibration Error (RMS, 7 keV)	*0.4 eV*
Count rate capability	*1 mCrab (> 80% high resolution events)*
Count rate capability (brightest point sources)	*> 30% throughput*
Time resolution	*10 us*
Non X-Ray background (2 – 10 keV)	*< 5 x 10^{-3} counts/cm^2/s/keV (80% of the time)*

Table 1.2: X-IFU top requirements

The production and test of the cryogenic anticoincidence detector is in charge to a collaboration made by the University of Genova and the Institute of Astrophysics and Planetology (IAPS) in Rome.

In particular, the Low Temperature Detector Group in Genova is responsible for the detector fabrication.

In the next sections, we will discuss the technology behind one of the most sensitive and promising detectors, focussing on the specific case of the anticoincidence. We will answer the question *“why is a cryogenic anticoincidence detector needed?”*, and show some results from previous prototypes. At last, we will show the actual progress status, with a discussion about the future development of the model to be flown for the mission ATHENA.

2. The Transition-Edge Sensor

A Transition-Edge Sensor (from now on simply TES) is a superconducting thin film used as an extremely sensitive thermometer, when it is kept within the narrow, almost linear region between its normal and superconducting states. It is a thermal detector, since the absorbed energy causes a rise in temperature of the TES, which we observe as a change in its resistance. When a thermal detector is used to measure the energy of individual photons/particles, it acts as a calorimeter. If the incident flux is too large to separate individual photons/particles, the detector is used to measure changes in the flux itself and it acts as a bolometer.

Calorimeters are able to link a temperature variation to an energy deposition. These devices are composed of two principal parts: the sensor (a TES, in our case), and an absorber, whose material depends on the event we want to measure (see Figure 2.1).

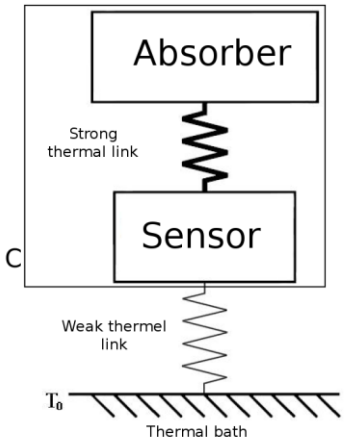

Figure 2.1: Calorimeter scheme.

A typical TES calorimeter is made of superconducting film hundreds of μm^2 in surface, with a metallic absorber grown onto it.

Typical working temperatures are around 100 mK, with a total heat capacity dominated by the metallic absorber, on the order of pJ/K. In this condition, an event with an energy of thousands of eV (nuclear recoils, soft X-Rays) causes the device to increase its temperature of hundreds of µK. This small ΔT can be detected efficiently with a TES due to its characteristic R(T), where a very small increment in temperature gives rise to a strong variation in its resistance, as we can see in Figure 2.2.

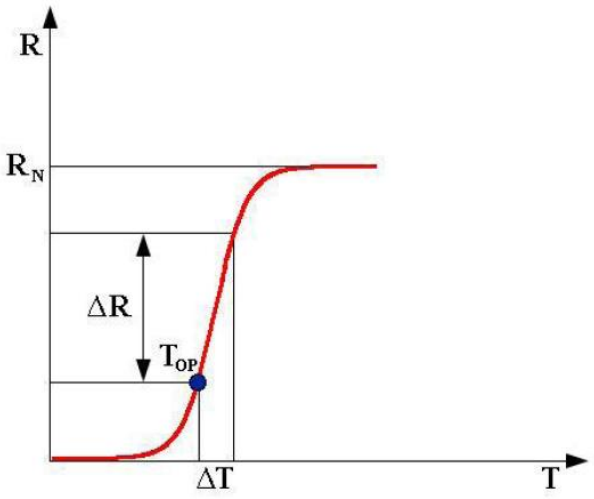

Figure 2.2: TES characteristic R(T). A TES is best operated in its linear region along the transition.

Usually, these microcalorimeters are manufactured in a clean room environment with micromachining lithographic techniques. The element used as superconductor depends on its transition temperature. There are some tricks to control the material bulk transition temperature, such as a proximization effect with a normal metal [18]. The element and the thickness of the absorber depends on the kind of effect we want to study: for instance, in X-Ray astronomy, 5 µm thick Gold absorbers are able to gather the entire incoming radiation [19].

First experiments using TESs were already conduced in the 1940's [20] [21]. There were many technical difficulties in managing this technology, for instance how to stabilize the detector and read the signal properly. A leap forward was made when Superconducting Quantum Interference Device (SQuID) current amplifiers made their debut [22] [23], providing an extremely sensitive, low noise readout that was also suitable for multiplexing. Another important step was the introduction of a voltage biasing circuit [24] [25], leading to a stable, self-regulating operation.

Basic TES calorimeter theory is well established [26], and many information regarding features and equations can be found in the cited reference. Here we present the main equations without going deep into details, describing the general thermal model and a particular application, of interest for this work.

2.1. General Thermal Model

A simple calorimeter model is shown in Figure 2.3. A TES with heat capacity C is connected to the heat bath at temperature T_s through a weak thermal link with thermal conductance G. Joule heating power P_j dissipated by the bias current helps keeping the TES at a steady state temperature $T_0 > T_s$. When an event (a photon or a particle hit) occurs in the absorber, with energy E_γ, the temperature of the TES rises by E_γ /C, and then relaxes to T_0 in a time given by the time constant $\tau = C/G$.

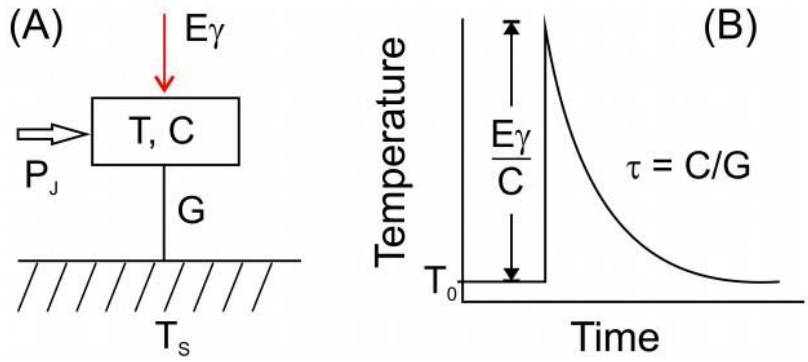

Figure 2.3: (A) Simple calorimeter model. (B) Temperature pulse caused by an event in the absorber

In Figure 2.4 the typical voltage bias circuit is presented, with its Thevenin representation. The starting point to describe our TES model starts by coupling two equations: one referring to the thermal dissipation, and one describing the electrical circuit (ignoring noise terms):

$$C\frac{dT}{ct} = -P_{out} + P_J + P_{in} \qquad 2.1$$

$$L\frac{dI}{dt} = V_{th} - I_{TES}R_L - I_{TES}R(T,I) \qquad 2.2$$

Where P_{out} is the power flowing out of the TES, via the heat link to the thermal bath, and P_{in} is the signal power. A power-law dependence is assumed for P_{out}:

$$P_{out} = K(T_0^n - T_S^n) \qquad 2.3$$

And the thermal conductance is defined as:

$$G \equiv \frac{dP_{out}}{dT} = nKT^{n-1} \qquad 2.4$$

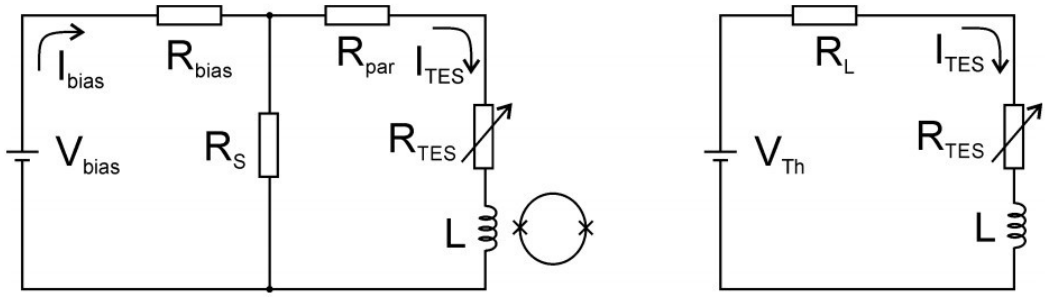

Figure 2.4: (LEFT) circuit used to bias a TES. R_{par} indicates any unwanted parasitic resistance in the circuit. $R_S < R_{TES} << R_{bias}$. (RIGHT) Thevenin equivalent circuit. $R_L = R_S + R_{par}$ and $V_{th} = V_{bias}R_S/R_{bias}$.

Since the resistance of a TES is a function of both temperature and current, R(T,I), we define two dimensionless parameters that describe the steepness of the superconducting transition.

$$\alpha \equiv \frac{\partial log R}{\partial log T}\Big|_{I_0} = \frac{T_0 \partial R}{R_0 \partial T}\Big|_{I_0} \qquad 2.5$$

$$\beta \equiv \frac{\partial log R}{\partial log I}\Big|_{T_0} = \frac{I_0 \partial R}{R_0 \partial I}\Big|_{T_0} \qquad 2.6$$

We define α the temperature sensitivity and β the current sensitivity.

However, we can only measure the I-V curve characteristic of our detector, finding the parameter

$$\alpha_{tot} = \frac{T_0 \partial R}{R_0 \partial T}\Big|_{T_0} \qquad 2.7$$

Which includes both the effects of α and β. Special care should be made on the notation used for these parameters, since they vary from author to author.

A constant current low-frequency loop gain is defined as

$$\mathcal{L}_I \equiv \frac{P_J \alpha}{G T_0} \tag{2.8}$$

Next, we look into the relationship between the three steepness parameters: α_{tot}, α and β. We start by assuming that we are in a small signal regime, where the TES resistance can be expanded to the first order as:

$$R(T, I) \approx R_0 + \frac{\partial R}{\partial T}\delta T + \frac{\partial R}{\partial I}\delta I \tag{2.9}$$

Using Equations 2.5 and 2.6:

$$dR = \alpha \frac{R_0}{T_0} dT + \frac{R_0}{I_0} dI \tag{2.10}$$

Similarly, Joule power $P = I_0^2 R_0$ can be expanded:

$$P(R, I) \approx P_0 + \frac{\partial P}{\partial R}\delta R + \frac{\partial P}{\partial I}\delta I = P_0 + I_0^2 \delta R + 2 I_0 R_0 \delta I \tag{2.11}$$

$$dP = I_0^2 dR + 2 I_0 R_0 dI = \alpha \frac{P_0}{T_0} dT + I_0 R_0 (2 + \beta) dI \tag{2.12}$$

From which we solve for dI:

$$dI = \frac{dP - \alpha \frac{P_0}{T_0} dT}{I_0 R_0 (2 + \beta)} \tag{2.13}$$

If we now introduce the thermal conductances:

$$g_0 = n K T_0^{n-1} \tag{2.14}$$

$$g_S = nKT_S^{n-1} \tag{2.15}$$

And we also write the steady state Joule power as:

$$P_0 = K(T_0^n - T_S^n) = \frac{g_0 T_0}{n}(1 - \frac{T_S^n}{T_0^n}) \tag{2.16}$$

Defining:

$$\theta \equiv 1 - \frac{T_S^n}{T_0^n} \tag{2.17}$$

So that Equation 2.16 becomes:

$$\frac{g_0 T_0}{P_0} = \frac{n}{\theta} \tag{2.18}$$

Joule power can also be expanded as:

$$P(R, I) = P_0 + \frac{\partial P_J}{\partial T_0}\delta T_0 + \frac{\partial P_J}{\partial T_S}\delta T_S \tag{2.19}$$

$$dP_J = g_0 dT_0 - g_S dT_S \tag{2.20}$$

Combining Equations 2.13 and 2.20:

$$dI = \frac{(g_0 - \alpha\frac{P_0}{T_0})dT_0 - g_S dT_S}{I_0 R_0(2 + \beta)} \tag{2.21}$$

Inserting this into Equation 2.10 and requiring that the bath temperature T_s must be constant, we can write:

$$dR = (2\alpha + \beta\frac{g_0 T_0}{P_0})\frac{R_0 dT_0}{T_0(2+\beta)} \qquad 2.22$$

Rearranging Equation 2.22 we find the connection between α_{tot}, α and β:

$$\alpha_{tot} = \frac{T_0 \partial R}{R_0 \partial T} = \frac{2\alpha + \frac{n}{\theta}\beta}{2+\beta} \qquad 2.23$$

2.1.1. Negative Electrothermal Feedback

The voltage bias setup has several advantages that are useful while operating TESs [27]. For example, it makes the detector bias point more stable and speeds up the recovery from pulses. To simply describe how the negative electrothermal feedback (ETF) works, consider a TES that is biased in the transition. The system has reached a steady state where the input power from Joule heating of the bias current equals the power flowing out through the thermal link. When an event occurs, the TES heats up and the resistance starts to increase. Because the TES is voltage biased, the increasing resistance means that the current has to decrease in order to keep a constant voltage. Thus, the Joule power $P_j = I^2R$ is decreased, which partly compensates for the temperature increase due to the event, speeding the recovery back to the steady state. The effective time constant due to ETF is given by:

$$\tau_{eff} = \frac{\tau}{1 + \alpha\,\theta/n} \qquad 2.24$$

Which shows that a TES will become faster as α becomes larger.

2.1.2. Energy resolution

For calorimeters, the most important figure of merit is the energy resolution. Assuming Gaussian noise sources, it is given by [28]:

$$\Delta E_{FWHM} = 2\sqrt{2\ln 2}\left(\int_0^{\infty} \frac{4}{S_{P_{tot}}(f)}\,df\right)^{-1/2} \qquad 2.25$$

S_{Ptot} is the total power referred noise that includes all noise sources and is given by:

$$S_{P_{tot}}(\omega) = \frac{S_{I_{tot}}(\omega)}{|S_I(\omega)|^2} \qquad 2.26$$

Where $S_{Itot}(\omega)$ is the total current noise. If the excess noise can be described with the M parameter, a useful approximation is given by [29]:

$$\Delta E_{FWHM} = 2\sqrt{2ln2}\sqrt{\frac{4k_B T_0^2 C}{\alpha}\sqrt{\frac{nF(T_0, T_{bath})(1+M^2)}{1-(T_{bath}/T_0)^n}}} \qquad 2.27$$

2.2. Silicon Absorber for Protons Detection

What we have described in the previous section is a simplified model for a typical TES. Real models keep tracks of small physical aspects related to the low temperature environment. One of the most important things to take into account is the thermal decoupling between the electronic and the lattice contributions, which is due to the different thermal conductance. One more peculiar effect is the Andreev reflection [30], which doesn't allow electrons to jump between normal – superconductor interfaces, and is useful to describe the thermal behaviour when dealing with normal absorbers in contact with a superconducting thermometer.

Consider, for instance, an Iridium TES thermometer, in contact with a gold absorber, directly deposited onto a Silicon Nitride substrate, which is in good thermal contact to the bath. This is represented in Figure 2.5 (LEFT), and it is one

of the simplest sample of TES system. If we want to write down its model, considering different thermal conductance for the electron and lattice systems, taking into account other physical phenomena, we must use the scheme in Figure 2.5 (RIGHT), where every term is decoupled and shown.

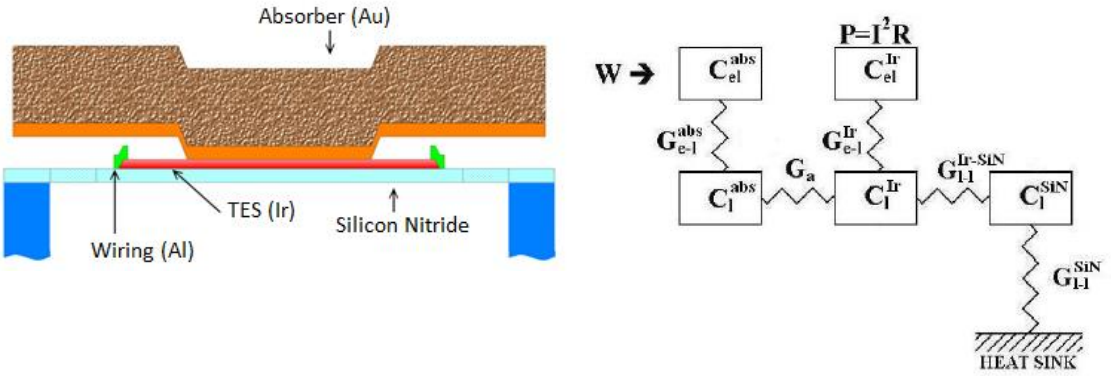

Figure 2.5: (LEFT) typical TES configuration cross-section view. (RIGHT) related block scheme.

In this scheme, one must consider the different coupling factors for every term: typically, there's a strong *e – e* and *ph – ph* coupling (electronic and lattice respectively), while the cross term *e – ph* is proportional to T^{β}, where β may vary between 4 and 5, depending on the purity and crystalline structure of the material [31], and also we have to consider the Kapitza resistance between absorber and TES, proportional to T^3 [32].

One should take care in modelling its own system, since many other parameters may be added: proximizing a TES with a normal metal on it will add new terms for both electronic and lattice system and so on.

We now want to focus on a particular TES system, which is of interest for our studies: The substrate is now crystalline Silicon, and TESs thermometers are deposited on it. While it holds the TES system, it also acts as absorber for incident radiation. A sketch and its block diagram are shown in Figure 2.6:

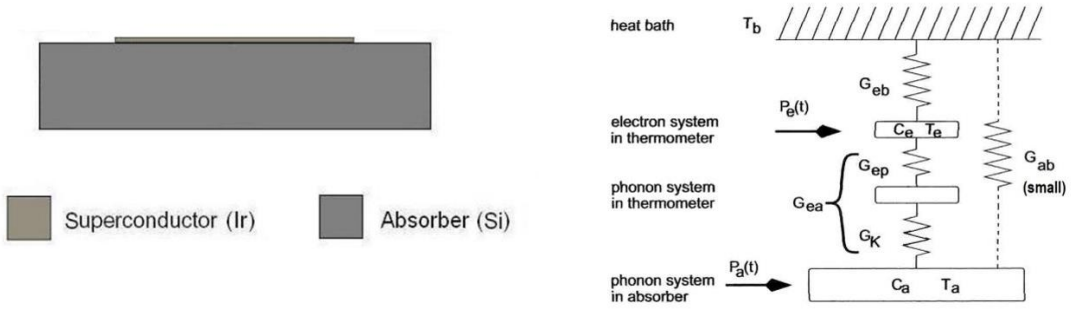

Figure 2.6: (LEFT) TES with Silicon absorber and (RIGHT) its block diagram.

This is a particular calorimeter setup, which we use as the baseline configuration for our detector inside the ATHENA project.

When an event occurs in the Silicon absorber, e.g. a high energetic protons hits, the crystal is excited by ionization. Lattice keeps electron back in place, so they start vibrating, propagating a lattice wave along the crystal, otherwise known as phonons. This is due to the bands inside Silicon (Figure 2.7).

Phonons travel along the crystal in a time scale $\tau \sim L/c$, where L is the dimension of the Silicon crystal, while c represents the wave speed inside the Silicon, being on the order of 8400 m/s: in a crystal 1 cm long, it all happens in about 1 µs. This is known as athermal phonon, and represent the first event happening inside the crystal. Athermal phonons decay anharmonically, giving rise to a thermalization of the lattice itselef, which heats up: thermal phonons.

Since the absorber is a semiconductor, the thermal coupling between TES and absorber is given by:

$$G_{Ta} = \left(\frac{1}{G_K} + \frac{1}{G_{ep}}\right)^{-1} \qquad 2.28$$

Where G_K represents the Kapitza term at the absorber-TES interface proportional to T^3, while G_{ep} stands for electronic – phononic coupling, proportional to T^5.

The input power $P_e(t)$ in Figure 2.6 is due to athermal phonons propagating inside the TES. These thermalize in the electronic system, and may “flow” through the

conductance G_{eb} (contribution given by the readout wires, usually negligible) to the thermal bath. They won't be transferred to the Silicon absorber due to the negligible coupling *e* – *p*. This effect causes a decrease in the population of thermal phonons in the absorber, coming from athermal phonons in the TES. For the same reason, athermal phonons in the crystal may thermalize on the absorber surface, giving a contribution $P_a(t)$ to the thermal phonons population [32].

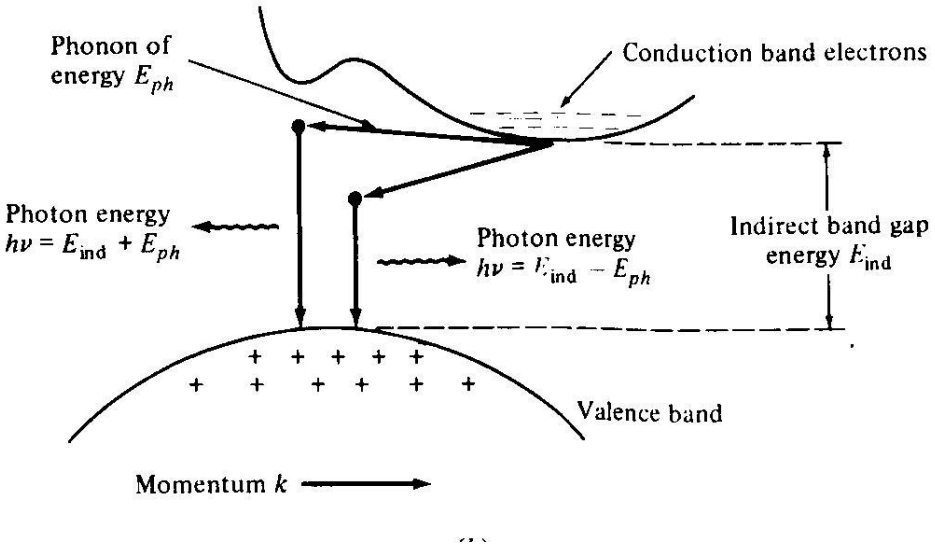

Figure 2.7: A photon absorbed in Silicon would produce a phonon due to the presence of a non-direct gap

2.2.1. Pulse Shape

The lifetime of the thermal pulses $\tau_{t,TES}$, is essentially given by the G value between the absorber and the TES. It corresponds to the thermal relaxation time in the absorber. To find the relaxation time of the athermal pulse, $\tau_{nt,TES}$, we must consider two contributions:

$$\tau_{nt,TES} = \left(\frac{1}{\tau_{film}} + \frac{1}{\tau_{crystal}}\right)^{-1} \quad 2.29$$

Reference [32] shows a simple model to find τ_{film}:

$$\tau_{film} = \frac{2V_a}{A_{TES}\bar{\eta}\langle v_{g\perp}\alpha\rangle} \quad 2.30$$

Where V_a is the absorber volume, A_{TES} is the TES total area, $\bar{\eta}$ is an absorption probability coefficient of athermal phonons inside the TES, while the term $\langle v_{g\perp}\alpha\rangle$ is the product of the athermal phonons group speed normal to the separation surface between absorber and TES, times the transmission probability of athermal phonons, mediated over all the oscillating modes and wave vectors of the incoming phonons.

In the same reference, there are some estimated values for these parameters, for Iridium TES on Silicon absorber.

If the surface/volume ratio of the crystal is small, or the percentage of surface covered by TES is big enough, one can approximate Equation 2.31:

$$\tau_{nt,TES} \simeq \tau_{film} = \frac{2V_a}{A_{TES}\bar{\eta}\langle v_{g\perp}\alpha\rangle} \quad 2.31$$

Energy deposition can be described in the following:

Athermal phonons relaxate inside the TES, with the input power:

$$P_e(t) = \Theta(t)\epsilon\left(\frac{E}{\tau_{nt,TES}}\right)e^{\frac{t}{\tau_{nt,TES}}} \quad 2.32$$

Thermal phonons relaxates inside the absorber, with the input power:

$$P_a(t) = \Theta(t)(1-\epsilon)\left(\frac{E}{\tau_{nt,TES}}\right)e^{\frac{t}{\tau_{nt,TES}}} \qquad 2.33$$

Where $\Theta(t)$ is the step function, while ε is the fraction of athermal phonons absorbed inside the TES. We assume that the energy exists at one instant in the form of athermal phonons in the absorber crystal. This assumption leads to a set of differential equations with solution ΔT(t):

$$\Delta T(t) = \Theta(t)\left[A_{nt}\left(e^{\frac{t}{\tau_{nt,TES}}} - e^{\frac{t}{\tau_{in,TES}}}\right) + A_t\left(e^{\frac{t}{\tau_{t,TES}}} - e^{\frac{t}{\tau_{nt,TES}}}\right)\right] \qquad 2.34$$

Where the quantities before the brackets are the partial heights of the two contributions, athermal and thermal. The other terms represent, respectively:

- Athermal phonons lifetime in the absorber, fast time constant:

$$\tau_{nt,TES} = \left(\frac{2V_a}{A_{TES}\bar{\eta}\langle v_{g\perp}\alpha\rangle}\right)^{-1} + (\tau_{crystal})^{-1} \qquad 2.35$$

- Intrinsic time constant depending on the TES properties:

$$\tau_{in,TES} = \frac{C}{G_{Ta} + G_{eb}} \qquad 2.36$$

- Lifetime of the thermal phonons inside the absorber, slow time constant:

$$\tau_{t,TES} = \frac{C}{\frac{G_{eb}G_{Ta}}{G_{eb}+G_{Ta}} + G_{ab}} \qquad 2.37$$

Figure 2.8 shows the signal resulting from the combination of the two components. The athermal contribution is given by the rise time $\tau_{in,\mathrm{TES}}$, and the

decay time $\tau_{\mathrm{nt,TES}}$, while the thermal term is given by the rise time $\tau_{\mathrm{n,TES}}$ and the decay time $\tau_{\mathrm{t,TES}}$. When in ETF regime, $\tau_{in,\mathrm{TES}} \ll \tau_{\mathrm{nt,TES}}$ and, hence, the pulse can be described by one rise time and two decay times.

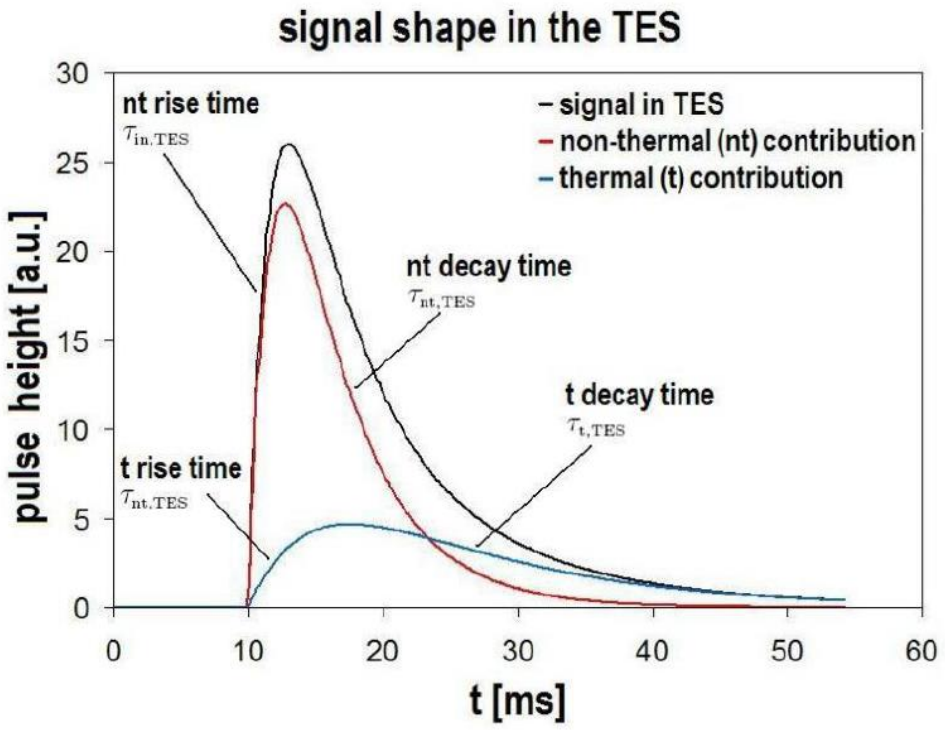

Figure 2.8: Signal pulse in a Silicon absorber TES (black), sum of two components: athermal (red) and thermal (blue).

3. The Anticoincidence Detector

The need of an anticoincidence detector arises since L2 background is full of high energetic particles [33]. From simple calculations, we can observe that GeV protons are MIP -in the minimum of ionization- for the metallic absorber of the main X-Ray array. That is: the energy deposited is of the same order of magnitude of the soft X-Rays we want to measure (Figure 3.1).

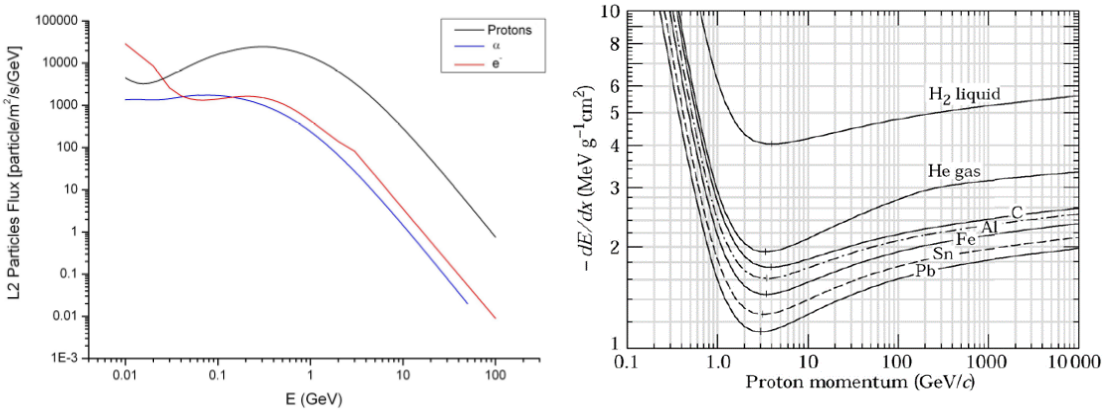

Figure 3.1: (LEFT) L2 particle flux expected. (RIGHT) Bethe-Bloch function showing GeV protons behaviour as MIPs.

What differentiate a true soft X-Ray from a MIP is the fact that the main array TESs are made to fully absorb 0.1 – 10 keV X-Rays, while any other source of energy will pass through, causing a double event (see Figure 3.2).

Several Monte Carlo simulations have shown that this setup can widely improve the effectiveness of the X-Ray detection, enabling the mission goals of ATHENA [34].

The same simulations provide us the main parameters for the anticoincidence manufacturing: first of all, the active volume must be placed 1 mm below the main array, and should have an accurate timing resolution to enable a correct trigger on the fake event. Moreover, its detection threshold must be above 10 keV and below the minimum energies deposited by background particles [35].

The total area should be very large though, and the edges of the detector should override those of the main array, to account for particles coming with some tilt angles.

More specifications will be shown in Section 3.2.

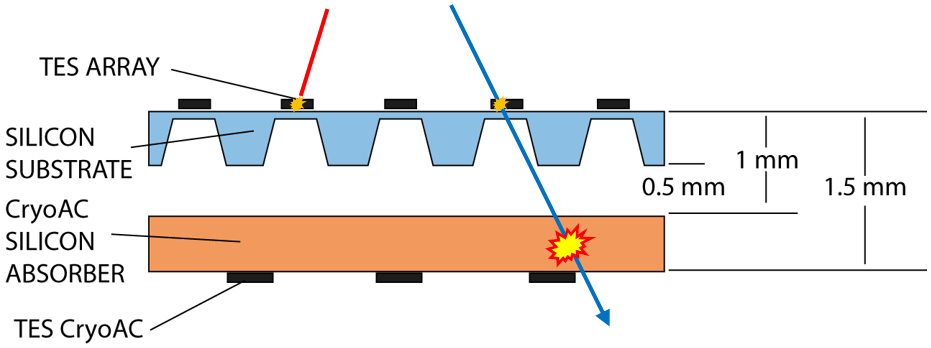

Figure 3.2: Working principle of our anticoincidence detector. X-Ray photons (red) are likely to be completely stopped at the main X-Ray array, while other background particles (hard X-Rays, protons, etc.) are too energetic to be absorbed. An anticoincidence detector helps discriminating these fake events (blue).

3.1. The Background Question

Compared to other energy bands, X-Ray wavelengths suffer from higher unwanted background, since they usually show low fluxes and, hence, need higher observation times.

Signal to Noise Ratio (SNR) will always consider not just the source statistical fluctuations, but must take into account also background.

The background adds poissonian fluctuations to the total counts, reducing the SNR [36]:

$$SNR = \frac{S}{\sqrt{N}} = \frac{S}{\sqrt{N_S + N_B}} \qquad 3.1$$

Where N_S and N_B are source and background noises.

In any X-Ray satellite we find two components in the background: and internal particles one and a diffuse X-Ray component. The first is generated by particles traveling through the hull, releasing energy inside the detector. This effect leads to the generation of secondary particles, mostly electrons and fluorescence photons.

The second component is known as Soft X-Ray Background (SXRB), which consists of a diffuse, isotropic X-Ray emission in the 0.1 – 10 keV band, reaching the detector thanks to the optics focusing.

We can write an expression to get the minimum detectable flux F_{min} [36]:

$$F_{min} = \frac{n_\sigma}{QA_{eff}} \sqrt{\frac{B_p A_d + Q j_d \Omega A_{eff}}{t \Delta E}} \qquad 3.2$$

Where t is the observation time, Q the detector quantum efficiency, ΔE the instrument energy bandwidth, Ω the angular size of the source, A_{eff} and A_d are the area of the instrument and the physical area of the detector, and B_p [cts cm^{-2} s^{-1} keV^{-1}] is the internal particle background, while j_d [cts cm^{-2} s^{-1} keV^{-1} sr^{-1}] is the diffuse X-Ray background.

From Equation 3.2 it is clear how the background level degrades the detector capability. The diffuse X-Ray component is not easy to reduce, so the only way is to act directly on the particle background, in order to enhance the detectable flux.

There is poor knowledge about the particle background in L2. ATHENA will be the first mission adopting microcalorimeters to operate at that orbit.

We know there are two main contributions to the background: the first component is made of cosmic particles with galactic origin (GCR), mainly protons, α-particles

and electrons, whose energy is in the range 10 MeV – 100 GeV. At this level, they can penetrate the satellite hull and also generate swarms of secondaries.

The second component comes from solar activities (solar protons), and strongly depends on the solar activity itself.

Figure 3.3 shows the latest estimations about the background counts on the X-IFU assembly. We expect a particle level of about 3.1 cts cm^{-2} s^{-1}. Using an active anticoincidence detector, together with some software discrimination, and other precautions, its level is reduced by more than an order of magnitude, down to 0.2 cts cm^{-2} s^{-1}.

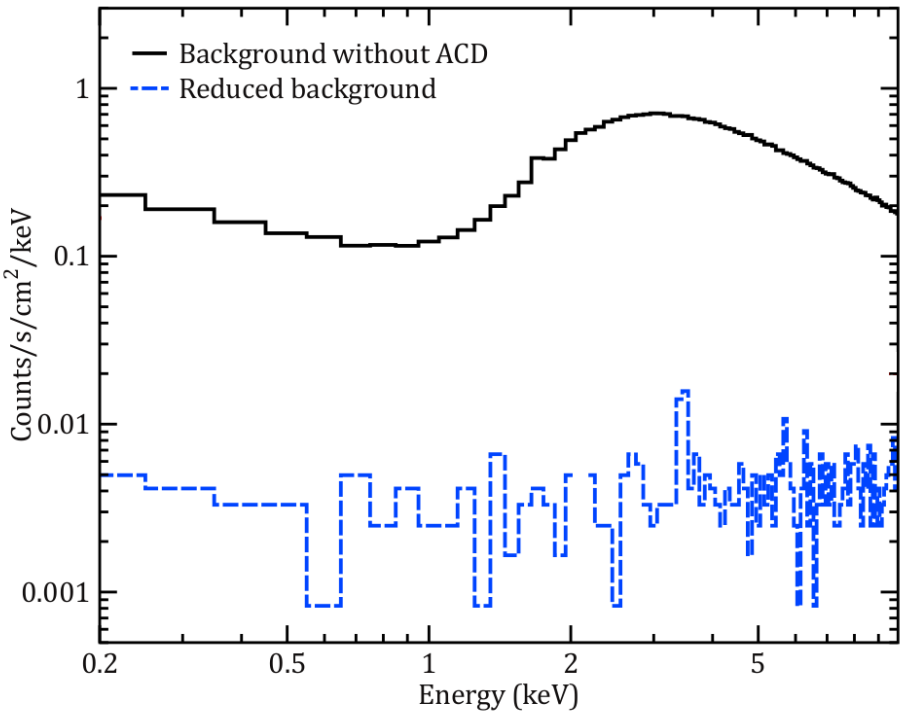

Figure 3.3: Spectra of the background expected at the detector level, coming from Monte Carlo simulations. The black line is what we expect without any anticoincidence, while the blue line takes into account the presence of an active anticoincidence detector, with pattern recognition algorithms and the insertion of a kapton layer to reduce secondary emissions.

3.2. The Cryogenic Anticoincidence CryoAC

To fulfil the request on the detection efficiency and, hence, on the background rejection, the anticoincidence detector must be very close to the main X-Ray array, 1 mm below. For this reason, adopting a cryogenic solution is an easy way. The problem arises when dealing with large areas, TES based detectors. We need to collect the signal over a wide surface, with a fast timing.

Our baseline consists in a detector made of Silicon, divided in 4 pixels, each covered by tenths of TESs. Each Silicon pixel is the sensing area, which gather the signal to heat up the TESs. Despite the same technology, the advantage of using Silicon as a converter substrate is the chance to operate in an athermal, non-equilibrium, regime, providing a faster response with respect to traditional TESs, which operate at thermal equilibrium instead.

Table 3.1 summarizes the main requirements needed for the CryoAC, as given by general requirements which can be found in [37].

Parameter	***Value***
Total effective rejection efficiency (primaries)	*99.9% (TBC)*
Total effective rejection efficiency (secondaries)	*99.9% (TBC)*
Low Energy Threshold	*12 keV (TBC)*
Detector Dynamic Energy Range	*2 keV – 600 keV (TBC)*
Data Acquisition Dyamic Range	*0 keV – 1 MeV (TBC)*
Time tagging accuracy	*10 μs (TBC)*
Time tagging resolution	*TBD*
Intrinsic deadtime	*1% @ ≤9.15 cts/cm^2/s (TBC)*
Induced deadtime towards TES array	*TBD*

Table 3.1: Anticoincidence requirements.

Moreover, these specifications require the detector geometry to follow what is listed in Table 3.2:

Parameter	***Value***
Number of pixels	*4*
Pixel size	*1.15 cm^2*
Absorber thickness (Silicon)	*500 µm*
Distance from main array	*≤ 1 mm*
Rise time	*≤ 30 µs*
Effective fall time constant	*≤ 250 µs (TBC)*
Thermal time constant	*≤ 2.5 ms (TBC)*
TES material	*Ir/Au*
Absorber material	*Si*
Transition temperature	*75 – 100 mK (TBC)*
Thermal bath temperature	*50 – 55 mK*
TES normal resistance R_n	*10 – 20 mΩ (TBC)*
TES working point resistance	*0.1 – 0.2 R_n*
Slew rate	*≤ 50 A/s (TBC)*

Table 3.2: CryoAC specifications.

Linking together all these information, we arrived to the definition of what we call the Flight Model, that is, the design we will likely adopt for our cryogenic anticoincidence detector, whose structure (the Silicon support and pixels) is shown in Figure 3.4, for a thickness of 500 µm.

Every pixel, sustained by bridges each, is 1.15 cm^2 in area, for a total coverage of 4.6 cm^2, higher than the X-Ray array (2.6 cm^2). More information will be discussed in Section 4.

Upon each pixel, a number of TESs will be deposited with microlithographic techniques, to manufacture the sensing part. They will be made of an Ir/Au bilayer.

Four SQuIDs, one for each pixel, will read out the signal generated by the TES network due to an event occurring on one of the pixels.

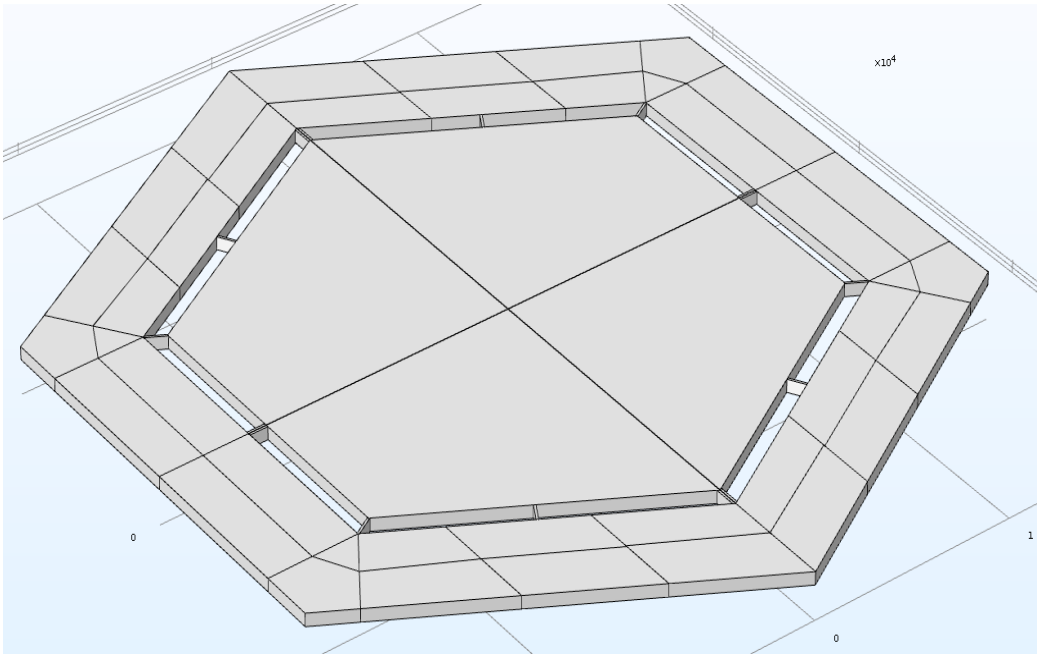

Figure 3.4: CryoAC CAD model (Silicon absorber + support structure only).

3.3. AC-S#: What Has Been Done

Long before ATHENA could reach its actual status, several samples have been tested in the framework of an X-Ray satellite, whose first name was IXO (International X-Ray Observatory).

Since then, we have been studying the behaviour of TES detectors grown over Silicon crystals, in order to find the best solution to gather as much signal as possible over wide areas. Figure 3.5 shows a short of the history of the sample produced in the laboratory facilities of Genova, called AC-S#, where the # stands for the sample number.

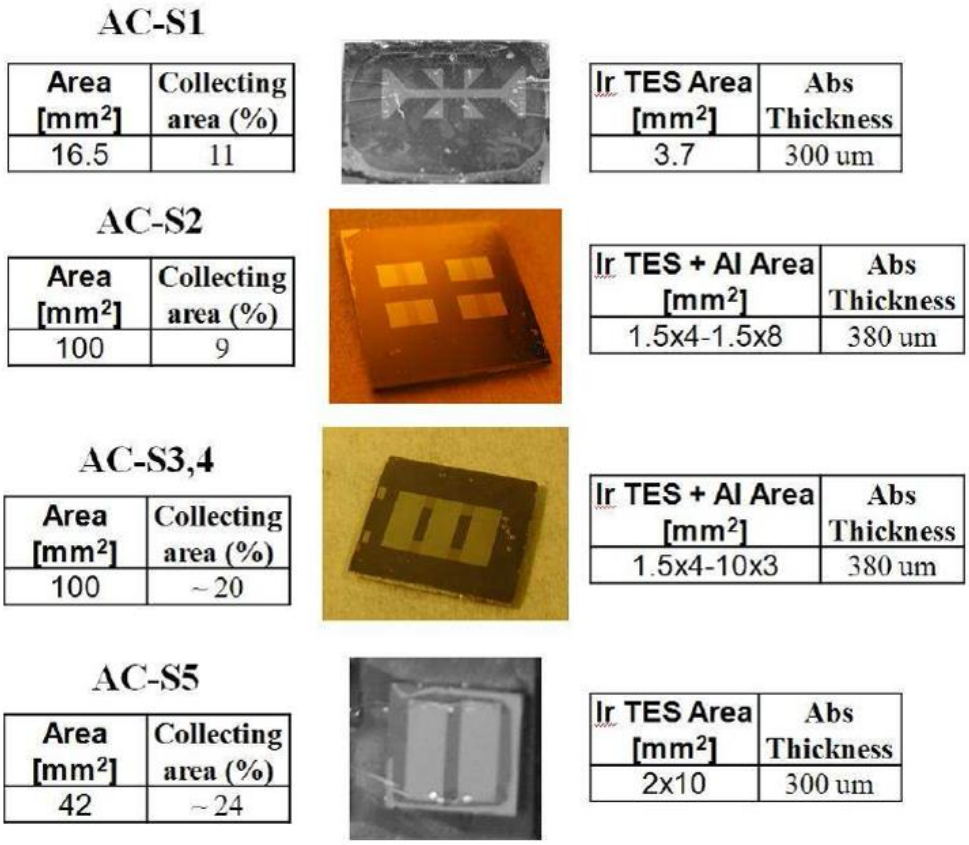

Figure 3.5: Samples studied since now.

With AC-S1 we got a simple Iridium TES over a Silicon substrate. Its response was one of the fastest. It was somehow the forefather to our activity in studying phonon-mediated TESs [38] [39].

As we wanted to increase the detector area, also the need to increase the TES coverage came, so the next samples were born. They were the mix to gain more and more surface coverage, as a trade-off with keeping the Iridium heat capacitance negligible with respect to the Silicon crystal.

Aluminium was also considered to improve the total area coverage: it is a superconducting material whose transition temperature is higher than that of the Iridium TESs, guaranteeing an even wider surface covering, with a total heat capacity still dropping faster.

Diffusivity is defined as:

$$D \equiv v_{Fermi} \times L_{freepath} \qquad 3.3$$

In Al its value is about 0.01m^2/s [40], so quasi-particles should take few microseconds to cover 1mm of length.

From all the TESs developed, we found two main aspects:

- Need of high surface coverage
- Low volume TESs
- Possibility to use Aluminium to improve collecting area, keeping low heat capacitance

The next two samples tried to put a milestone in the search for the perfect TES based, athermal gathering anticoincidence detector.

3.4. AC-S7, AC-S8. A Milestone Deep Analysis

Figure 3.6 shows the latest two detectors produced and long studied, AC-S7 and AC-S8. They are the natural evolution of the detectors developed since now, joining together a large detection volume, with TESs spread all over the surface, uniformly gathering the athermal signal developing inside the Silicon volume.

Table 3.3 summarizes the main parameters of both detectors.

They are made of a Silicon absorber, 1cm^2 in surface, and 380 μm thick. 65 Iridium TESs are uniformly grown over its surface, and are read-out in parallel configuration, by means of a Niobium wire. AC-S7 foresees the use of Aluminium finger-like structures, whose role is that of gather as much signal as possible, enhancing the total are coverage. Thermal conductance is controlled by 4 connection towers, lithographically shaped and filled with an epoxy glue, whose thermal conductivity is known, ensuring a good control and reproducibility of this important parameter.

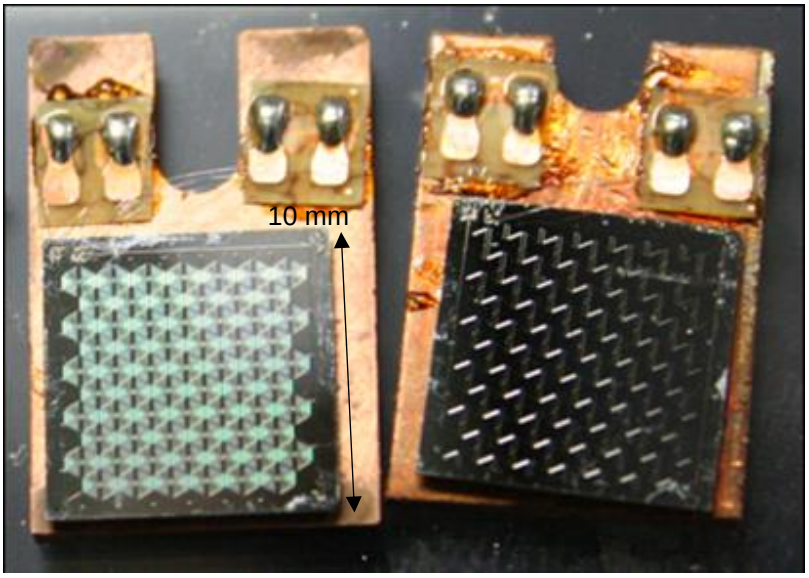

Figure 3.6: AC-S7 (RIGHT) and AC-S8 (LEFT), bonded and mounted on their copper holder.

AC-S7 and AC-S8 characteristics	
Absorber material	*Silicon [100]*
Absorber area	*10 x 10 mm²*
Absorber thickness	*380 µm*
TES material	*Iridium*
TES number	*65*
TES area	*100 x 100 µm²*
TES thickness	*200 nm*
Wire material	*Niobium*
Total collecting area (TES)	*0.65 %*
Total collecting area (TES + fingers)	*~50 %*
Epoxy towers (LxWxH)	*500 x 500 x 50 µm³*

Table 3.3: AC-S7 and AC-S8 main parameters

3.4.1. Fabrication Processes

Both detectors share the same production process.

It starts with the cut of a commercially available Silicon wafer (our sample was a [110] Silicon 1-20 Ωcm in resistivity) in small squares, 10 x 10 mm^2. Every square is used as an active chip, and will sense the incoming radiation.

From every chip, three processes take place: at first, we deposit a thin layer of Iridium by pulsed LASER deposition technique, using our Nd:YAG LASER. The total thickness is about 200 nm, obtained from previous calibrations of the apparatus. To ensure a good uniformity, the sample holder is rotated in different positions. The thickness is measured and confirmed after finishing, using an optical profilometer.

Second step, a positive lithography is made, patterning the Iridium surface with the 65 TESs, which we obtain after ion-milling the chip with Argon DC plasma sputter.

This way we obtain 65 Iridium TESs uniformly covering the starting Silicon surface.

A negative lithography shapes the readout wiring, connecting all the TESs. We then evaporate Niobium using a RF sputter. Later profilometer measures confirmed that every TES was contacted by the Niobium film.

For AC-S8 only, one more step is required: a negative lithography to shape the Aluminium collectors, which are then evaporated using a thermal evaporation source.

These steps complete the active chip with TESs thermometers and their readout. The next step is the preparation of 4 SU-8 permanent photoresist towers to manufacture the thermal conductance: they are rigid walls empty structures, with the inner part filled with EPO-TEK 301-2 epoxy glue, which has a well-known thermal conductivity [41]. They are prepared with the same lithographic techniques, onto a second Silicon chip, a buffer which will be used to contact the whole detector to the thermal bath. After the preparation, the first active chip is mounted over the 4 towers. The EPO-TEK 301-2, after 1 hour of bake over a hot plate, becomes solid, ensuring a stable structure.

Figure 3.7 shows a sketch of the processes here described; Figure 3.8 shows a detail of both active pixels produced; Figure 3.9 shows a sketch cross view of the detector, and a detail of the conductance towers. Table 3.4 summarizes some parameters for the manufacturing.

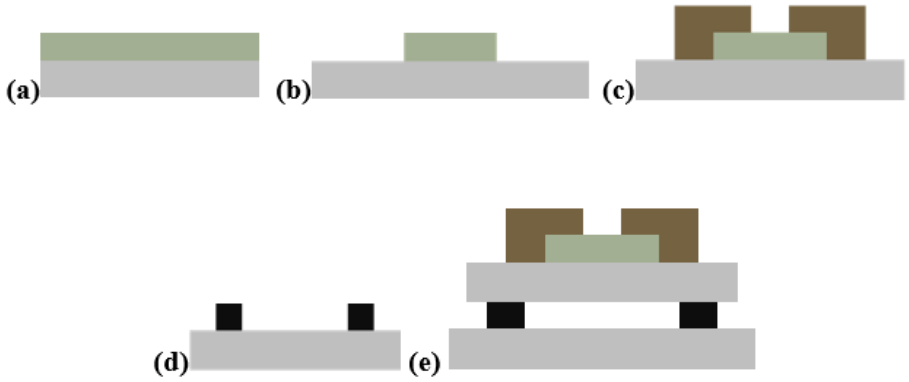

*Figure 3.7: Fabrication process: **(a)** iridium film deposition by pulsed laser deposition; **(b)** film patterning by positive photolithography and dry etching; **(c)** niobium wiring deposition and patterning by negative photolithography, RF-sputtering and lift-off process; **(d)** SU-8/epoxy tower building on buffer chip; **(e)** active and buffer chip coupling.*

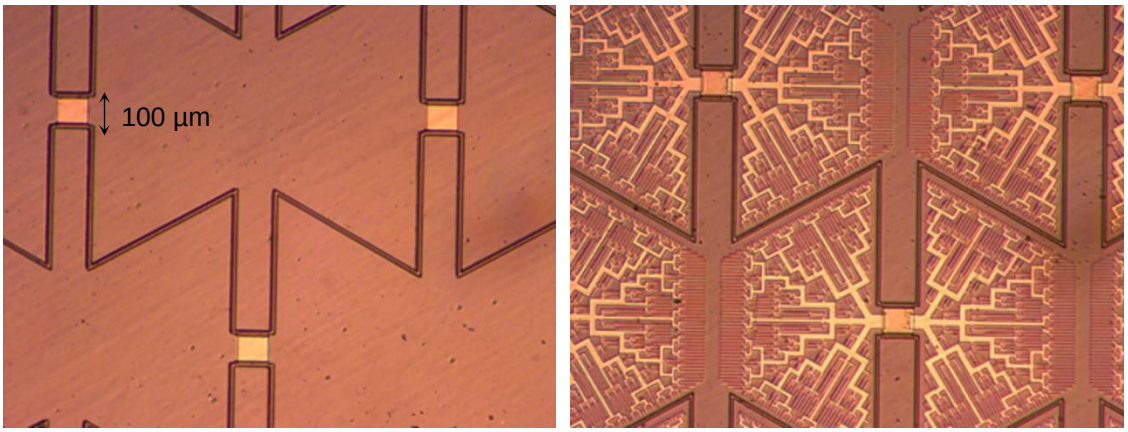

Figure 3.8: 4x magnification detail of both detectors, AC-S7 on the LEFT, AC-S8 on the RIGHT. Three out of the 65 Ir TESs are visible, with their connecting Nb wirings (darker lines). On AC-S8 the Al fingers structures are well visible, contacting every TES.

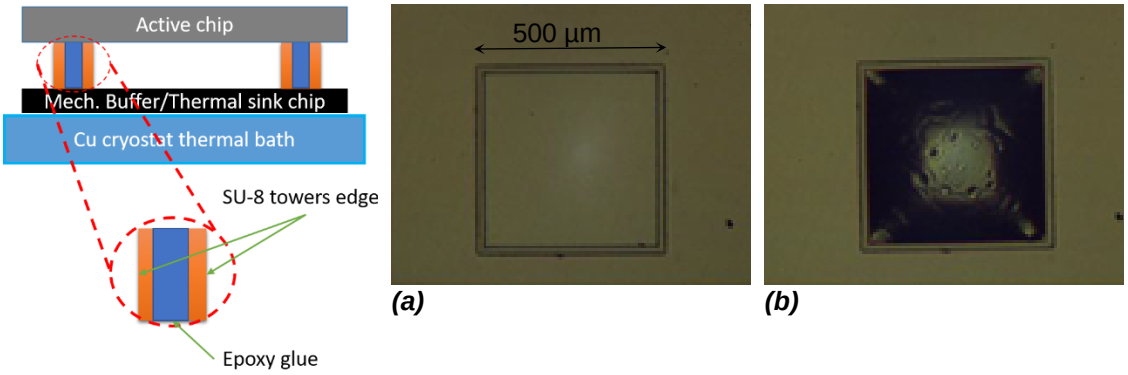

*Figure 3.9: (LEFT) sketch cross view of the complete detector. (RIGHT): SU-8 walls empty **(a)** and filled with EPO-TEK 301-2 **(b)***

AC-S7 and AC-S8 manufacturing	
PLD vacuum	*10^{-9} mbar*
Ir thickness	*200 nm*
Photoresist (positive)	*ma-P 1240*
DC sputtering vacuum	*3 x 10^{-6} mbar*
DC argon equilibrium	*2 x 10^{-2} mbar*
DC sputter power	*30 W*
Photoresist (negative)	*ma-N 440*
RF sputter vacuum	*2 x 10^{-8} mbar*
RF sputter argon equilibrium	*5 x 10^{-2} mbar*
Nb thickness	*870 nm*
Evap vacuum	*2 x 10^{-6} mbar*
Al thickness	*500 nm*
EPO-TEK total conductance (4 towers)	*2 x 10^{-8} W/K*

Table 3.4: Some manufacturing parameters

3.4.2. Detectors Characterization

Several measurements were made on the two detectors. First of all, we characterized them to check for important parameters, such as the normal resistance at room temperature, the TESs circuit resistance after the transition of Niobium only, and finally the transition temperature curve of the thermometers themselves. Next, I-V characteristics have been profiled, and finally a spectral analysis to probe for the detection performances.

AC-S7 has been extensively studied at our laboratories in Genova, and at our collaborators in Rome. Results showed a very good reproducibility of the main parameters, which is important too.

Figure 3.10 shows the two setups, used in Genova, to measure the R(T), the I-V characteristic, and the response to incoming radiation.

R(T) was obtained using a four wires setup, using a Model 5210 Lock-in amplifier by Princeton Applied Research, while for I-V curves and for radiation response, we used a setup with different SQuID sensors: a SUPRACON VCBlue model,with

an input coil inductance of 350 nH for the I-V curves, and a VTT SQuID with 2 nH input coil inductance to measure the detector spectra.

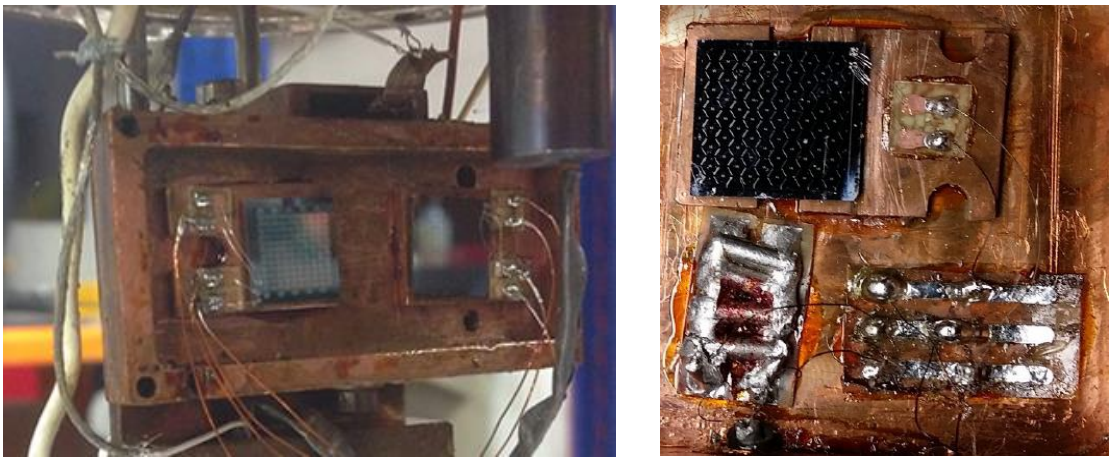

Figure 3.10: (LEFT) R(T) measurement setup. (RIGHT) SQuID measurements setup

All the measurements done in Genova were made in an Oxford Kelvinox 25 dilution fridge.

The transition temperature of AC-S7 is shown in Figure 3.11. It is about 124 mK, with a transition width of 2 mK. The sample normal resistance is about 1.4 mΩ, but we found some 30% discordance between the resistance measured this way and with a SQuID setup.

For AC-S8, as measured in Rome, we found a slightly different value for both the transition temperature and the normal resistance, as can be seen in Figure 3.12. Since they have been measured in different periods, it may depend on some setup variations along the gap. Its normal resistance is approximately 2 mΩ, and its transition temperature is around 120 mK, with a transition width of 2 mK.

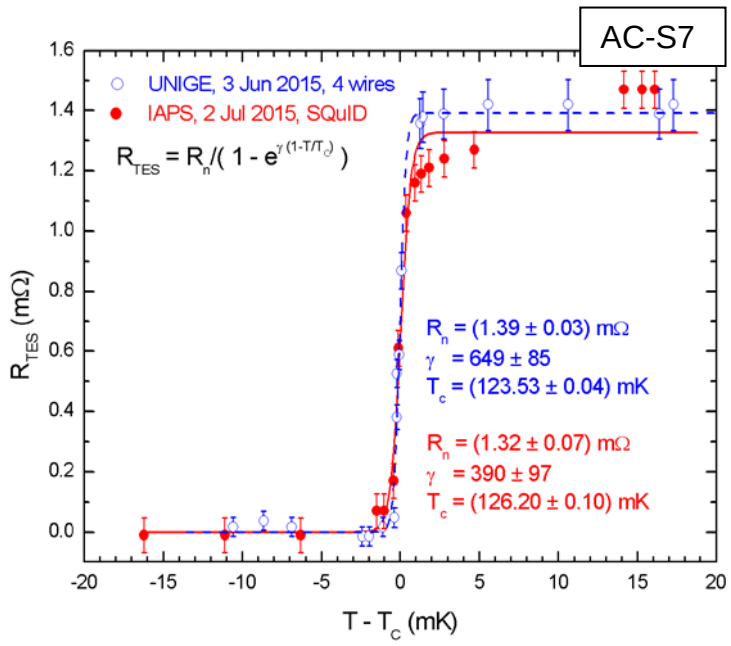

Figure 3.11: Comparison between R(T) characteristics for AC-S7, obtained by Genova (Blue) and Rome (Red)

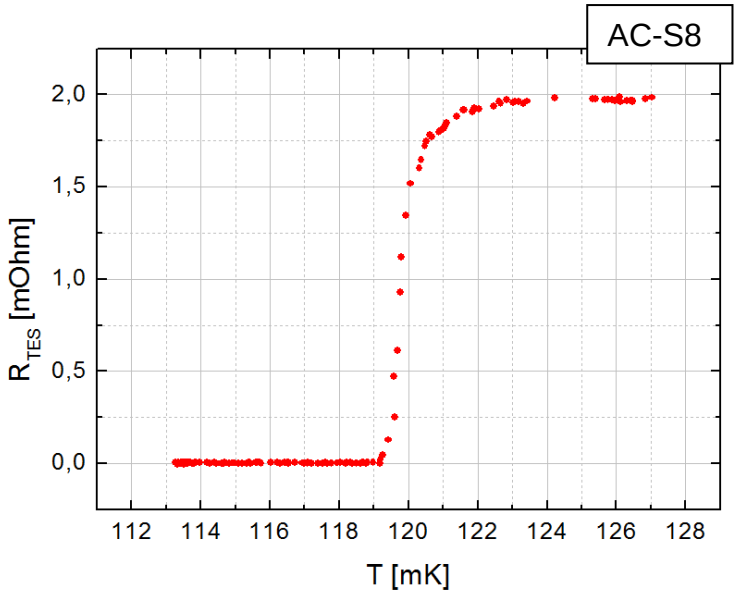

Figure 3.12: AC-S8 transition curve measured in Rome

Concerning the more interesting SQuID measurements, we used at first a SUPRACON VCBlue model, which we had in our stocks, for the first analysis. We then moved to a VTT SQuID after checking for the normal resistance of the TES samples: VTT will provide the read-out SQuID for the project, so they made

a SQuID for our purpose, with a lower inductance input coil, in order to set the cut-off frequency a bit far away from our detector response, improving the overall characteristic of the resulting pulses: the cut-off frequency, in terms of time response, is defined as:

$$\tau \equiv \frac{L}{R} \qquad 3.4$$

Since R is on the order of 2 mΩ, we obtain more or less 175 μs with the 350 nH inductance of the SUPRACON SQuID, and 1 μs with the 2 nH VTT inductance.

Figure 3.13 shows a simplified setup scheme, which represent the sketch of the partially-shown setup in Figure 3.10 Right.

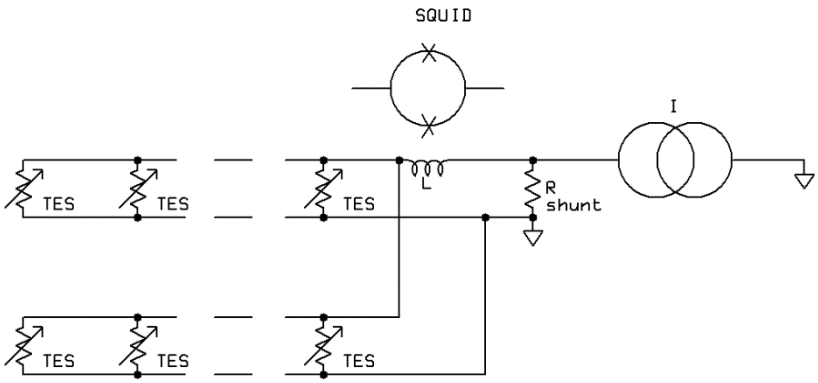

Figure 3.13: Setup scheme for AC-S7/8 SQuID read-out.

The SQuID amplification converts the current variations in a voltage signal. All the connection between shunt resistor, device and inductance are fully superconductive and have been previously tested:

- Nb/Ti wires have a superconducting transition at 9 K;
- $Pb_{60}Sn_{40}$ used for soldering has a transition around 7 K;
- Cu pads have a square resistance of about 10^{-6} Ωcm^2.

The overall parasitic resistance should be driven by Cu pads, but it is lower enough to allow for the measure, since the normal resistance of our detectors is

on the order of mΩ, the working point of the TESs should be 10% of the normal resistance, 100 μΩ.

The Shunt resistor was hand-made by mean of constantan wires, soldered in a parallel configuration with $Pb_{60}Sn_{40}$, for a total measured resistance of (140±1) μΩ at liquid Helium.

This is quite high, since is comparable to the working point resistance of our detector: the electrothermal feedback can suffer from unwanted variation in the circuit bias, and could explain the anomalies found in Figure 3.14, Blue line.

I_{bias} is measured reading the voltage drop across a calibrated resistance $R_{load} = (5.0018 \pm 0.0005)k\Omega$, with a differential measure acquired via National Instrument ADS. V_{out} is measured with the same ADC. Acquiring this value at different temperatures allows to know the TES resistance, according to the following equations:

$$V_{TES} = (V_{in} - I_{TES}R_{load})\frac{R_{shunt}}{R_{shung} + R_{load}} \qquad 3.5$$

Where V_{in} is the voltage across the load resistance, and I_{TES} is given by the following equation:

$$I_{TES} = \frac{V_{out}}{G_{SQuID}} \qquad 3.6$$

Where G_{SQuID} is the SQuID gain (250000 V/A measured for the VCBlue).

Our dilution fridge has a thermal stability of 10 μK. At each temperature, a set of I-V curves are automatically acquired via a LabView routine. The superconducting circuit is biased with an AC voltage with $f = 0.01\ Hz, V_{pp} = 10\ V$.

In Figure 3.14 a subset of I-V characteristics is shown. From a linear fit of the slope at low bias, we evaluate the resistance in the limit of zero current and zero dissipated power, allowing to reconstruct the R(T) curve, as shown in Figure 3.15, together with the calculated α of our detector. In this case, as told before, the

normal resistance appears to be a 20% higher than that measured by 4-wires setup.

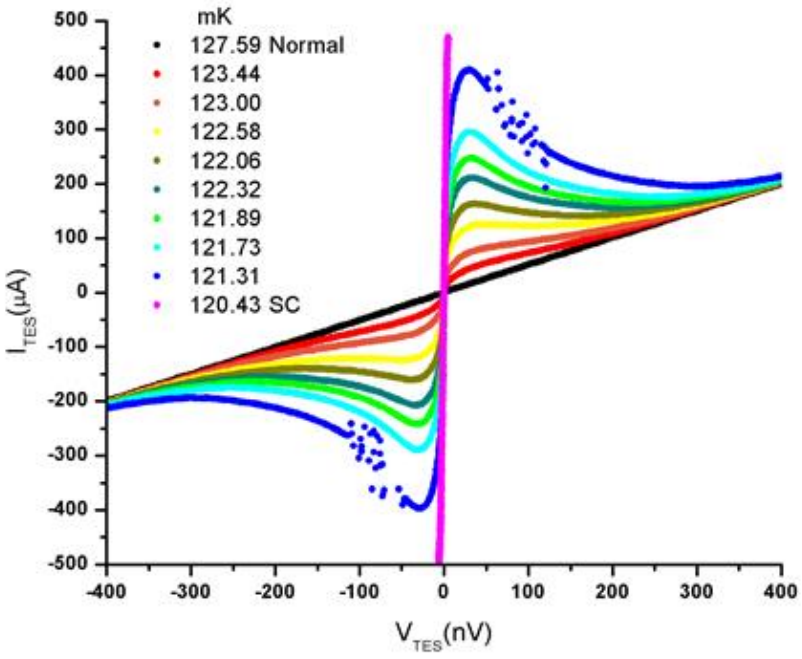

Figure 3.14: A subset of load curves I-V obtained at different bath temperatures.

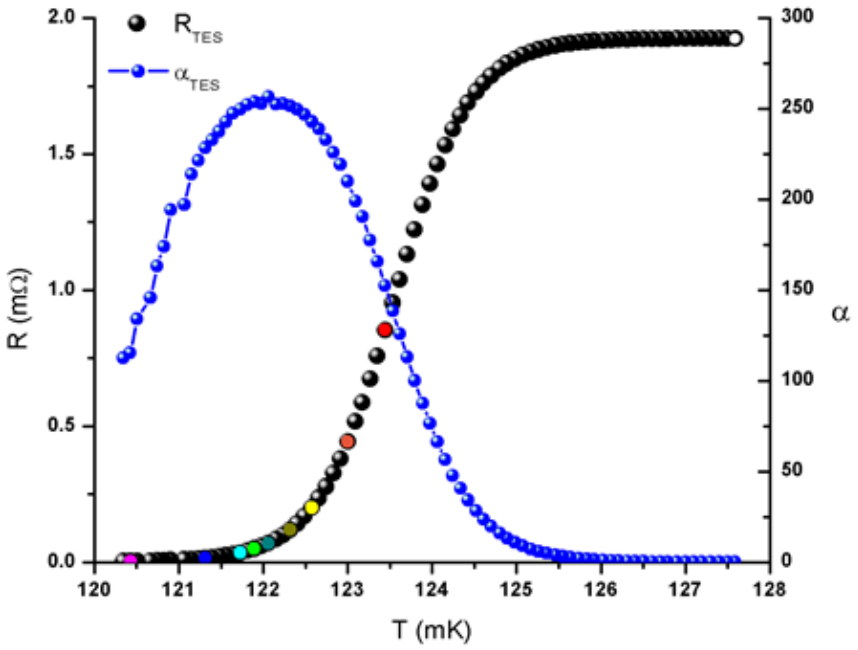

Figure 3.15: R(T) obtained by fitting I-V characteristics (coloured dots corresponds to each of the I-V curves of Figure 3.14), and α parameter calculated.

3.4.3. Pulse Detection and Energy Resolution

To test the energy resolution, simulating a particle event inside the absorber, an ^{241}Am was used. Americium has an α-decay, with a Q-value of 5697.81 keV, and $t_{1/2}$ = 431 years:

$$^{241}Am \rightarrow {}^{237}Np + \alpha \qquad 3.7$$

The isotope emits a 60 keV γ-ray with a branching ratio of 36%.

Our source has an activity A = 37 kBq. We placed the source about 7 cm far from the detector, outside the steel cap of the cryostat, which attenuates it by a factor 30. This way, considering the solid angle, we expect a total activity on our detector of about 10 Hz per cm^2 or less, which is a good test for our detector, since the real anticoincidence detector will experience the same event rate.

The TES was DC-biased, applying a constant voltage of 35 nV at a bath temperature of 121.5 mK. The power dissipated by Joule effect is around 1 pW. We are not able to discriminate where the pulse originates inside the Silicon absorber, but this is not strictly required for the mission purposes.

We used a LabView routine to acquire thousand pulses, setting a trigger at 0.2 V, a pre-trigger of 0.02 s and a total acquiring window of 0.08 s. Sample rate was 10 kHz.

A typical pulse is shown in Figure 3.16. The athermal behaviour was found only in about 6% of the total recorded pulses. This is in good agreement with the expected value for a Silicon absorber [42].

The athermal rise time component is 24 µs, the thermal one is 190 µs. The decay times are 340 µs and 12 ms respectively. As we can see, using the SUPRACON SQuID would have cut the rise time response, making our detector slower than it really is.

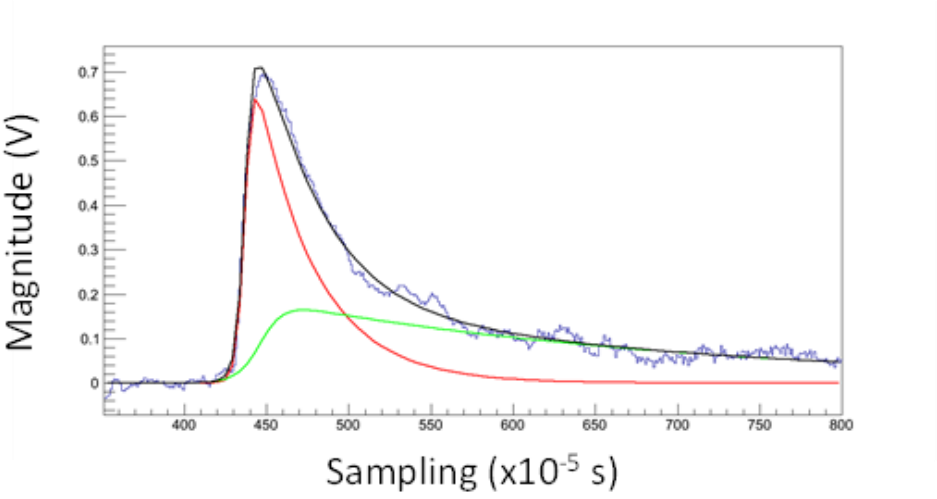

Figure 3.16: Typical pulse detected. Blue rusted line is the raw data acquired, Red line corresponds to the fit of an athermal component, while the Green line fits for a thermal component. The sum of athermal + thermal is represented by the Black line, which follows very well the original data, showing that our pulses are a superposition of both behaviours.

Pulses collected this way have been analysed in two different ways: in Genova, we set up a C++ program to analyse every pulses with athermal + thermal fit function and set up an Optimal Filter (OF) technique [43] [44].

In Rome, we used a Principal Component Analysis (PCA) to find the measured spectra. While it is costly in terms of resources power, it has the advantage of being model independent [45].

However, results are quite similar, the only difference is the estimation of σ: 9 keV @ 60 keV for the OF technique, while 4.8 keV @ 60 keV for the PCA, as shown in Figure 3.17 and Figure 3.18.

Moreover, with the PCA analysis it is possible to highlight another peak: this is most likely not to be a peak, but an edge instead, due to the high-energy portion of the Compton Edge resulting from Compton scattering in the sensor, a continuum from 0 keV to 11.4 keV, cut off at low energies. This is important to notice, since it means our detector has a low energy threshold around 10 keV, very close to that required for ATHENA, as already discussed in Table 3.1.

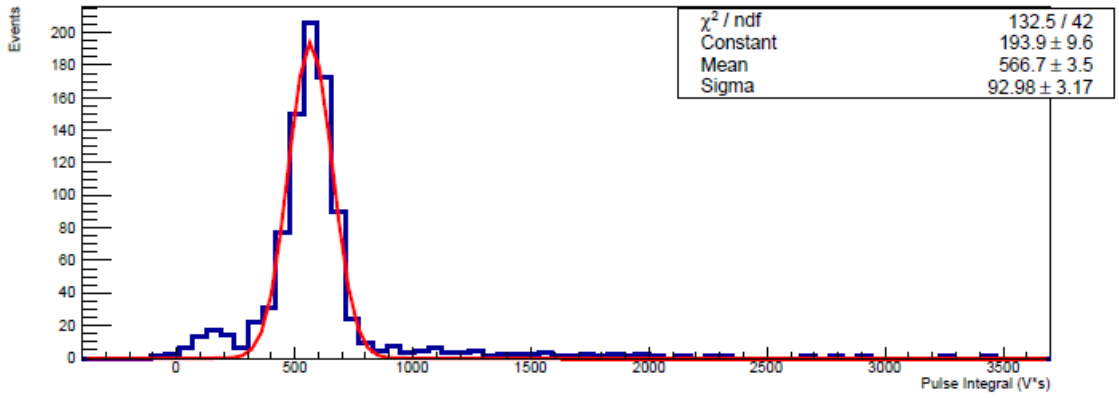

Figure 3.17: Reconstructed spectra using Optimal Filtering analysis. Assuming a linear behaviour, we find that the peak, corresponding to the 60 keV line of Am, has a standard deviation of about 9 keV.

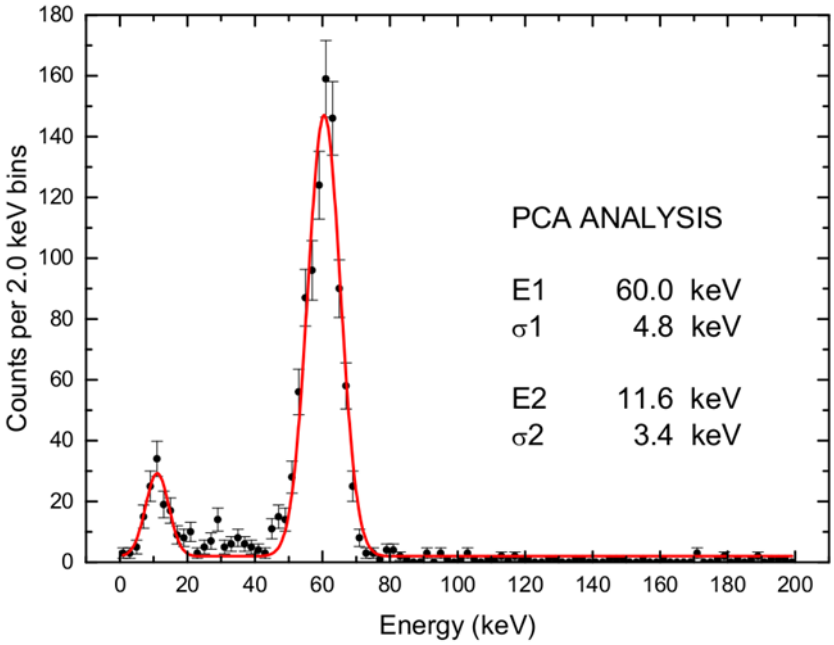

Figure 3.18: Reconstructed spectra using Principal Component Analysis. The resulting standard deviation is lower, and it is possible to distinguish a secondary bump, probably due to Compton scattering in the sensor.

The same analysis here reported has been conducted on AC-S8 as well, in Rome.

Unfortunately, this time the setup showed a parasitic resistance on the superconducting circuit, with a value of 2.5 mΩ, too high to set a good working point for the detector.

More analysis will be performed as soon as the setup will be fixed.

4. The Demonstration Model

The role of the previous models was to evaluate all the parameters we need for the final object flying on-board ATHENA.

As the end of the phase A is approaching, that is, the end of the R&D on all the components of the observatory, also the design of the focal plane is reaching its final shape, and so, the Anticoincidence detector has to.

The next phases will lead to what it will be called the Flight Model, with all the components integrated in the Focal Plane Array, as shown in Figure 4.1.

Following the simulations on background already discussed in Section 3, the structure will host the Anticoincidence detector to have a short gap with respect to the main TES array.

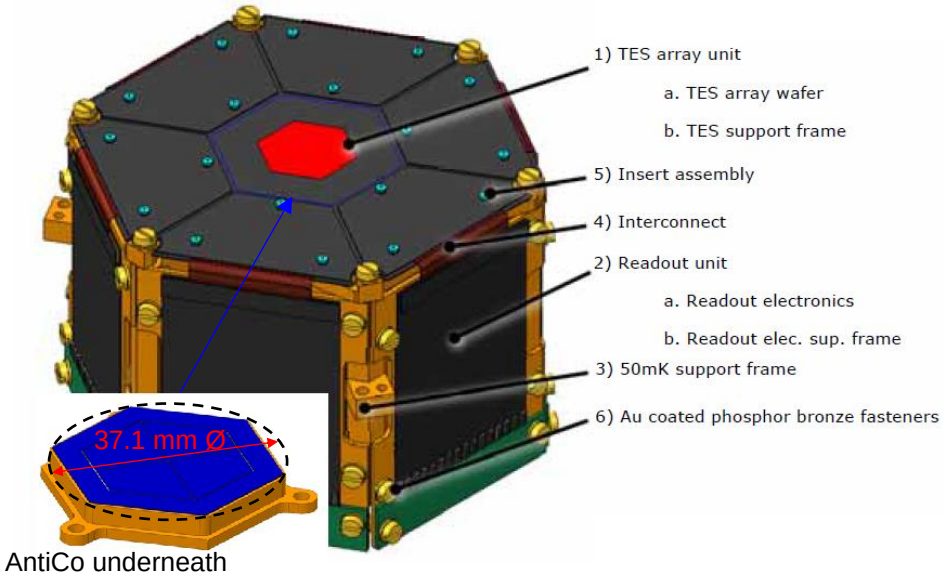

Figure 4.1: Focal Plane Array schematics. The Red hexagon represents the main TES array, while the Anticoincidence detector (Blue) is not visible since it will be placed underneath it, hidden by the overall structure.

Coming back to the Anticoincidence detector, the prototypes studied before need to be integrated in the solution adopted for the Focal Plane Array, and so we had to make changes in our structure, while consolidate and improving other aspects.

Having a bigger sample provides a higher thermal capacitance and so a higher energy limit. The use of many parallel-connected TESs allows to see more signals spread over a big volume, while keeping the thermometer heat capacity somewhat low. The use of glue is a risk in order to get a reproducible thermal conductance, which is essential for the microcalorimeter detection physics. Moreover, simulations show that a thickness of 500µm is a good trade-off for a good anticoincidence detector.

All these aspects previously studied brought us to develop a step-over sample: we call it CryoAC DM, which stands for Demonstration Model, as it will be the first of our objects to be tested together with main X-Ray array to probe their functionality together.

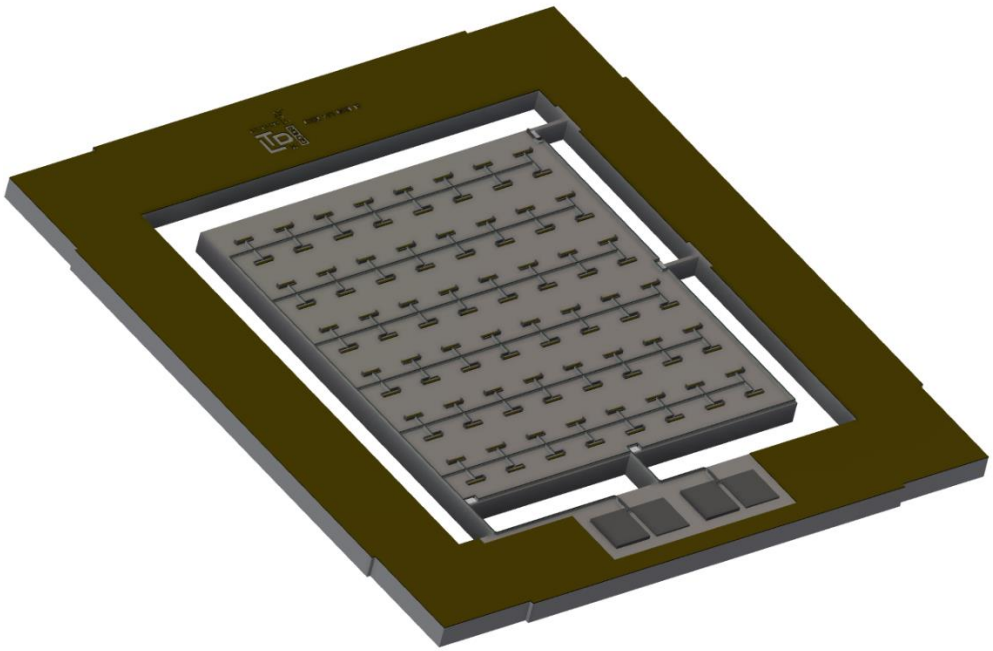

Figure 4.2: CAD rendering of the Demonstration Model. The gold-plated rim will be used to thermalize the entire structure. The leftmost bonding pads are the TESs signal reading, while the rightmost pads are the heaters power supply. 96 TESs, uniformly spread over the suspended active pixel, are read out in a parallel configuration.

Many features will be foreseen on the Demonstration Model and, hence, studied with the aim to find the best solutions for the Flight Model, which will be developed later.

It is made of a single monolithic silicon crystal, all micromachined to obtain the final shape. The DM is a 16.6 x 16.6 mm^2, 500µm thick, silicon piece, with a 10 x 10 mm^2 absorber suspended by mean of 4 bridges. The entire structure is obtained with a single Silicon etch process.

The outer region, the rim, is mainly covered with gold, and hosts the bonding pads, which will be used to make every electrical connection to the pixel. From the gold area, wire bondings will run to the thermal bath, to set the detector temperature uniformly. The wires develop along two bridges: one line, made of superposed, back and forth niobium films, is used to measure the TESs signal. The second one, with the same geometry and materials, powers 4 small heaters, made of platinum, which are used to set a temperature offset over the active area, the 10 x 10 mm^2 suspended pixel, which is the real sensing element, and represents roughly ¼ of the final planar dimension of CryoAC.

4.1. Design Motivations

A total amount of 96 rectangular TESs, 500 x 50 μm^2, 200 nm thick, are deposited over the surface of the active pixel. They are made of an iridium/gold bilayer, which is used to control the transition temperature of the superconducting iridium bulk (114 mK), and set it in a range between 75 mK and 100 mK, upon requirement. The normal resistance found for the previous samples, AC-S7 and AC-S8, with less TES connected, was very low (see Section 3.4.2). Due to the previous results, and since both gold and iridium have a very low resistivity, the normal resistance of the detector drops down to a very small value. Hence the use of rectangular-shaped thermometers.

The resistivity of bulk iridium is $\rho=4.7e^{-8}$ Ωm at room temperature, which means $3.1e^{-8}$ Ωm at liquid helium, considering a RRR of 1.5 [46]. For one single TES, we have therefore R=1.55 Ω. The 96 parallel TESs are then about 16 mΩ in normal resistance. Assuming the total thickness of the TESs will be 2/3 Iridium and 1/3 Gold, more or less we should still find the same value.

The use of niobium as wire is mainly due to manufacturing issues: aluminium (a widely used material for wires) is susceptible to basic developers used for production processes. Besides that, niobium is also a strong, resistant and higher Tc material. Like aluminium it forms a few atoms oxide layer over its surface, and this make it a strong and durable material. Two layers are grown, one above the other, with a silicon dioxide layer is in between, in order to enhance electrical isolation along the z axis. The use of a microstripline method [47] is useful to avoid magnetic loops, which could harm the main X-Ray detector above.

The small heaters, grown at the very edge of every of the 4 bridges, onto the suspended side, allow us to control the temperature of the pixel. Since the bath temperature will be of 50 mK, and our detector works better at higher temperatures, using only the bias current to dissipate more power (and heat the thermometers) could not be achievable for such a high gap. In addition, it could give us a less stable working point.

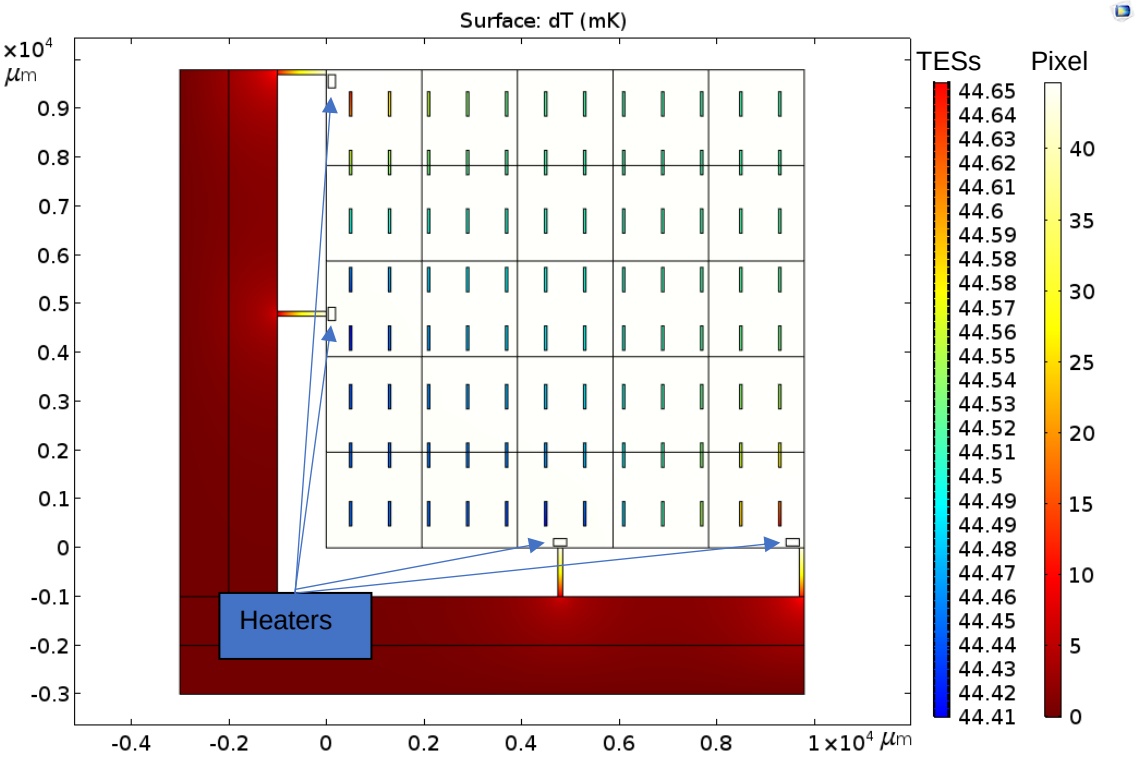

Figure 4.3: COMSOL simulation of a single pixel with a rim fixed temperature, and a constant power of nW applied on the four heaters (the four small pices at the end of each bridge, pixel side). We can see that the pixel area is well maintained at a higher temperature with respect to the rim, while the overall variation over the TESs, represented by small rectangular areas over the pixel, ranges from 44.41 mK to 44.65 mK.

Simulations, as it can be seen in Figure 4.3, show that using four heaters in this configuration could lead to a temperature offset as high as 50 mK in respect to the thermal bath, with a surface variation over the suspended pixel of maximum 240 μK.

Heaters are made of a meander-like platinum structure, 20 μm wide, 200 nm thick and 4 mm long. With an expected resistivity of about $4e^{-9}$ Ωm, we find 4 Ω per heater. At first order, considering a bridge thermal conductance G of $5e^{-8}$ W/K (see later), to set a 50 mK temperature gap we have to dissipate:

$$P = G\Delta T = 2.5\ nW \qquad 4.1$$

The use of micromachined bridges is not straightforward: their main role is to act as thermal link, and so their shape must be compliant with the calorimetric needs

in order to return a proper signal. However, they are the only connection to the rim and, hence, to the fixed part of the focal plane assembly. For this reason, they must be mechanically robust, in order to bear the active area of the detector avoiding breakages, sustaining stresses which especially occur during the launch phases.

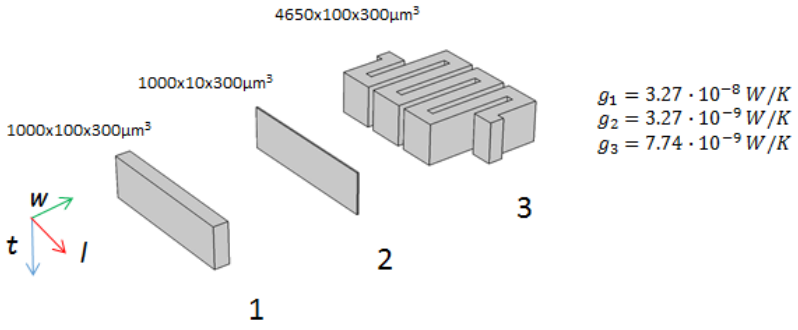

Figure 4.4: a set of bridges used for various simulations at first (note the 300 μm thickness, which was foreseen during the early stages of the DM design process). On the right side, their thermal conductance is estimated for a silicon truss.

For all these reasons, we run several simulations using COMSOL® Multiphysics and ANSYS® tools, in order to find the trade-off among all these parameters. The DM shape comes out from the first runs, while we kept simulating in order to improve every aspect.

Since the value of our thermal capacitance is fixed by the active sensing area pixel, whose geometry is strictly given by Monte Carlo simulations, we find out that the only way to control our signal shape only comes from the tight control of the thermal conductance.

As a general result, we found that the best trade-off solution foresees the use of four straight bridges, 1 mm long and 100 μm wide.

From previous models, we saw that a value on the order of $2e^{-8}$ W/K was suitable as a starting point to model our detector. This arises since, considering the low normal resistance value of our TESs and being the typical inductance of commercially available SQuIDs on the order of tens to hundreds of nH, we can

see that the R/L cut-off frequency sets our time constant on the order of tens of microseconds. To avoid any signal suppression, we should be above that value, say milliseconds. Being τ equal to C/G, having higher relaxation times means having a lower G.

From Figure 4.4 it is clear that we have two ways to reduce the thermal conductance: by either increasing the length of the bridges, or by reducing their section. Since the surface hosts the connection wires, we prefer to leave a width of 100 µm at least. As backup solution we foresee to use longer bridges, using a meander-like shape, in order to keep the same 2D dimensions of the final chip, with a conductance 4 times lower.

In the following we will show the results obtained for the straight geometry only, keeping in mind that we can eventually turning on the backup solution, which is in our reach, as shown in Figure 4.5.

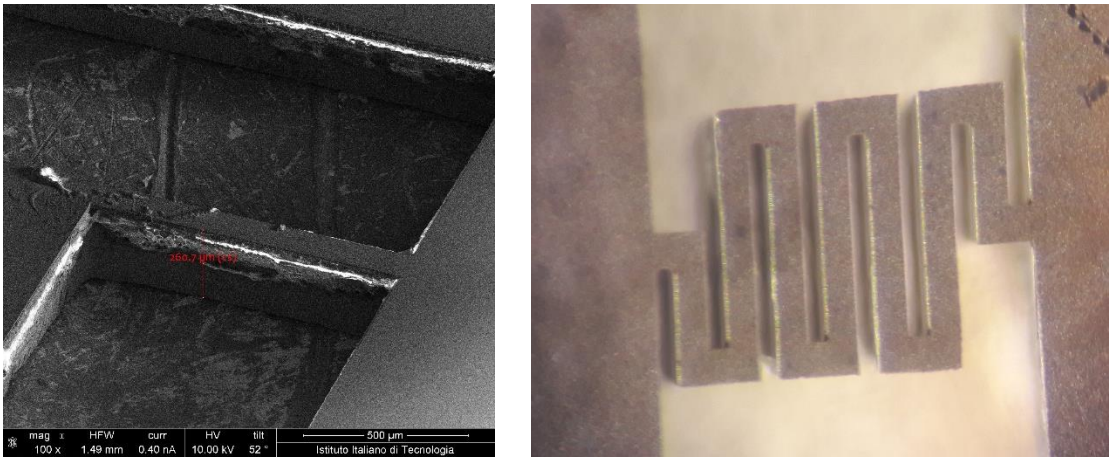

Figure 4.5: (LEFT) Scanning Electron Microscope image of a straight bridge sample produced at the Italian Institute of Technology. (RIGHT) optical magnification of a meander bridge sample produced in our laboratory after the upgrade of our Reactive Ion Etching machinery.

4.1.1. Thermal Simulations

The first parameter we took into account was the thermal conductance of our detector.

The particle hitting our Silicon chip releases energy by ionizing it over its thickness. Then, vibrations caused by lattice rearrangement decay and cause a thermalization. Of course, we didn't account for phonons propagation over the Silicon, since we wanted to check for thermal behaviours. We can assume the particle causes a heating of a very small volume, releasing a power of some tents of keV energy over less than 1 ps. So, our thermal simulation starts with a pulse-shape power dissipated in a very small volume of our detector.

Silicon thermal parameters were considered temperature dependant, in order to account for temperature variation during the pulse propagation. Thermal capacitance was evaluated using the Debye Law, using T_{Debye} of 647.9K for Silicon, so a trend following $(T/T_{Debye})^3$. For the thermal conductance, we extrapolated, down to 50 mK, data from a work of Sota et al. [48], for a same-trend law.

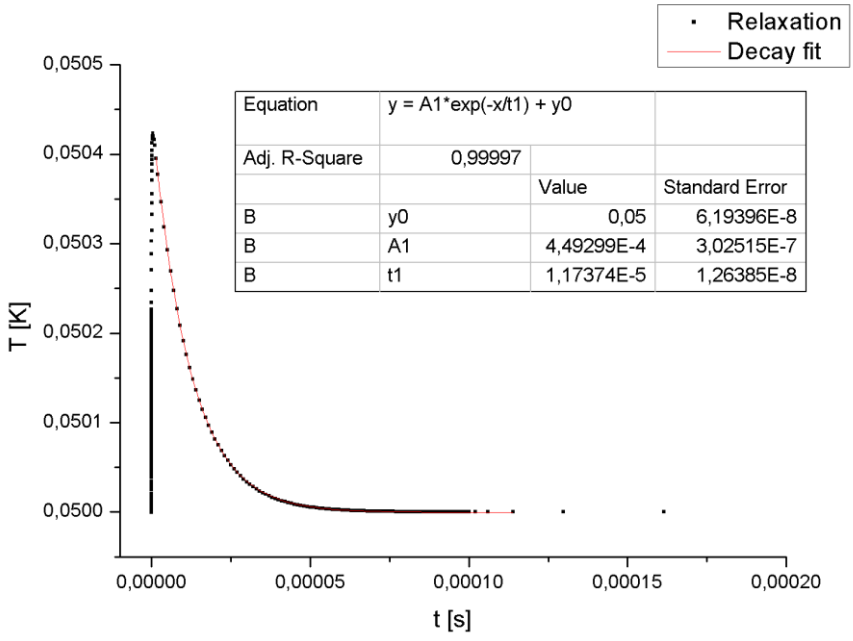

Figure 4.6: thermalization pulse, fitted with a typical decay exponential.

From Figure 4.6, we can see the resulting pulse obtained, fitted with a decay exponential law:

$$T(t) = T_0 + Ae^{-\frac{t}{\tau}} \qquad 4.2$$

Where T_0 is the base temperature, A is the pulse amplitude, and τ the thermal constant C/G, which is just at the cut off of our L/R circuit.

4.1.2. Mechanical Simulations

We run several mechanical simulations. At first, we focused on a simple square DM geometry, then, confident on the results, we moved to a shape more similar to that of the Flight Model, since the geometrical disposition of the bridges affects the mechanical behaviour of our detector more than the thermal response.

In Figure 4.7 the history of simulated structures is shown.

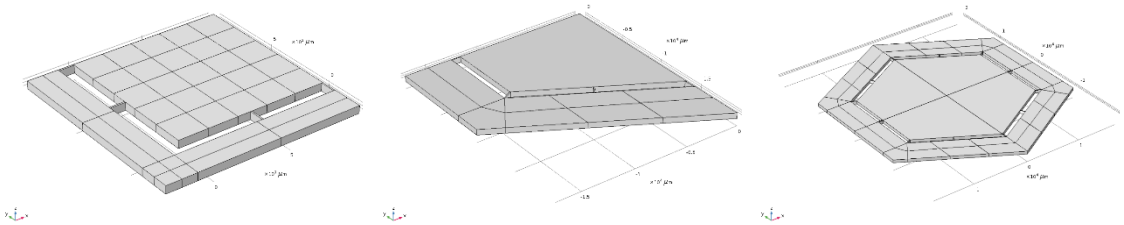

Figure 4.7: From Left to Right, single square pixel (DM-like); single trapezoidal pixel to fit a hexagonal detector; hexagonal detector made by 4 trapezoidal pixels.

In the following, we will show results concerning the Flight Model, since of most interest.

These are the simulations we took into account:

- Body load bearing up to 2000 G acceleration;
- Main eigenfrequencies; modal analysis to check for stresses;
- Random vibration analysis.

Three are the main constrains to consider our results satisfactory: 1) stresses inside our detector have to stay at least one order of magnitude below the known crystalline silicon yield strength breaking point [49]; 2) during acceleration forces or random vibrations, the maximum allowed displacement must be less than the gap from the main detector array (500µm); 3) eigenfrequencies should be far from resonances at which the focal plane will be stressed during launch phases. This last point is the most critical by now, since we only know that the launch vector will make use of a next generation Ariane rocket, which, at the moment, is nothing but a blueprint [50].

For the moment, we used a random vibration spectrum provided by CNES (Centre National d'Études Spatiales).

Our simulations are promising: below you can find the most interesting results, in which we can see some important aspects: first of all, the total displacement does not reach the total distance gap, even at very high accelerations (see Figure 4.8), and the total stresses on the four bridges for each pixel, is somewhat more than one order of magnitude below the breaking point of crystalline Silicon [49], as can be seen in Figure 4.9.

Concerning the detector eigenfrequencies and their relation to the frequencies of the focal plane, we can see from Figure 4.10, that the first value comes around 2.5 kHz, while the focal plane random spectra intensity falls down until 2 kHz.

As last simulation, we conducted a Power Spectra Analysis (PSA), using ANSYS software, to find the response to the given spectra in Figure 4.10 right.

The software highlights a maximum equivalent stress of 6 MPa, and a maximum displacement of 1.92 µm, as it can be seen in Figure 4.11 and Figure 4.12.

More details can be found in [51].

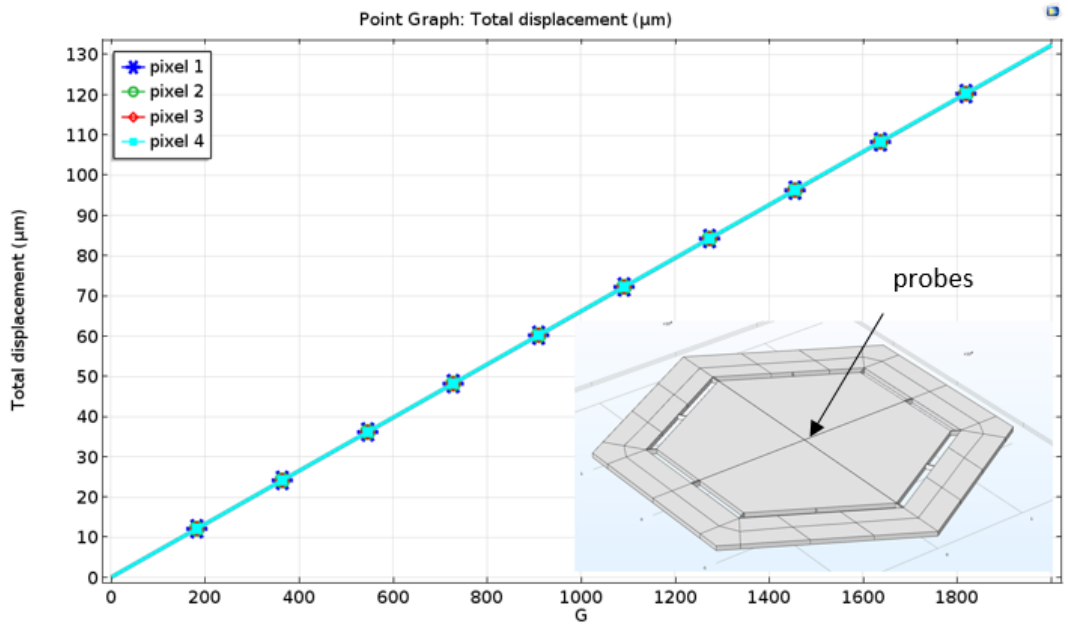

Figure 4.8: total displacement of the central points of the Flight Model, up to 2000G acceleration.

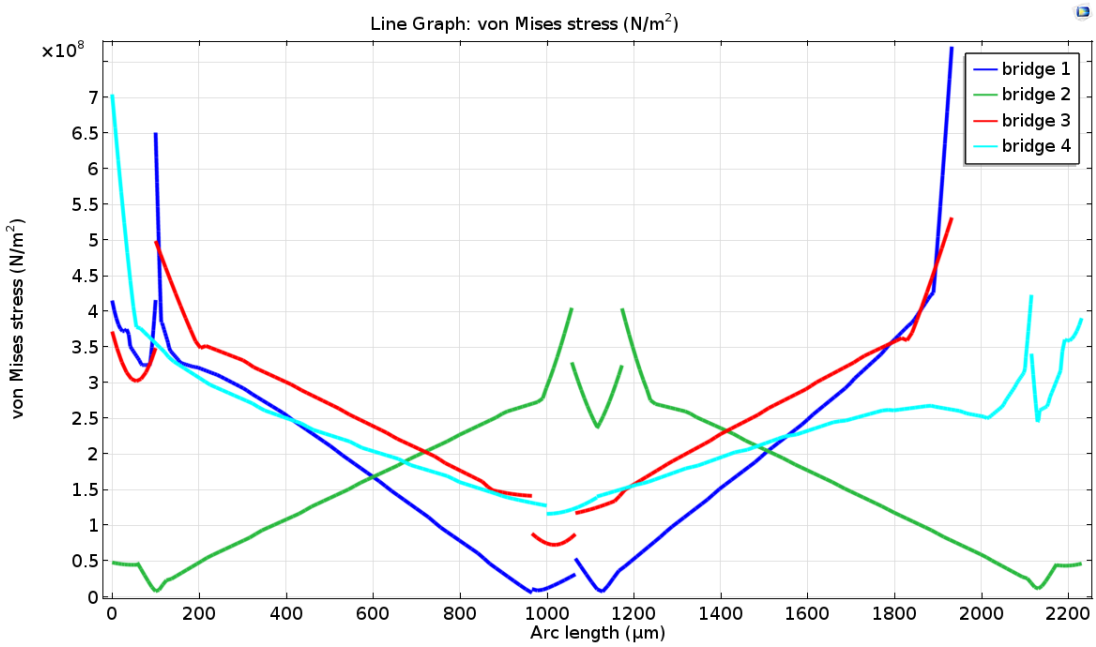

Figure 4.9: stress along each bridge for one pixel. The most critical point are those connected either to the rim or the pixel.

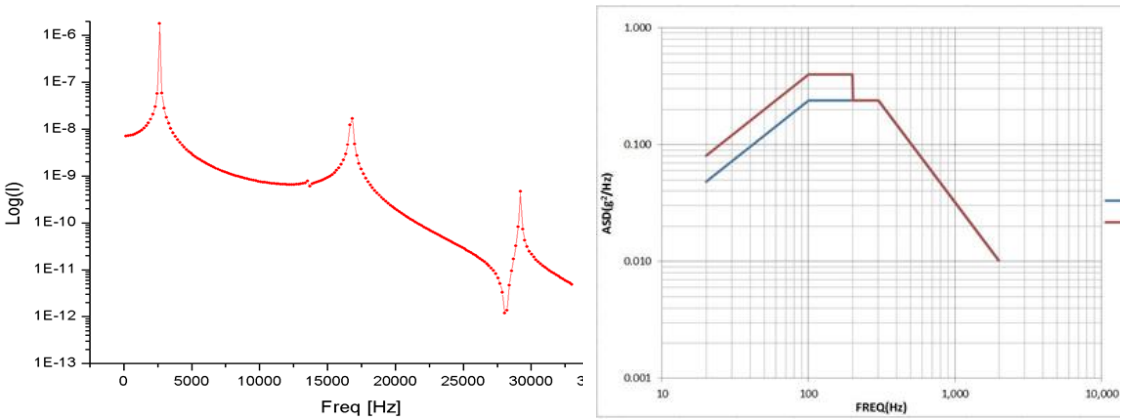

Figure 4.10: (LEFT) eigenfrequencies found for our detector. (RIGHT) reference spectra used for our random vibration analysis.

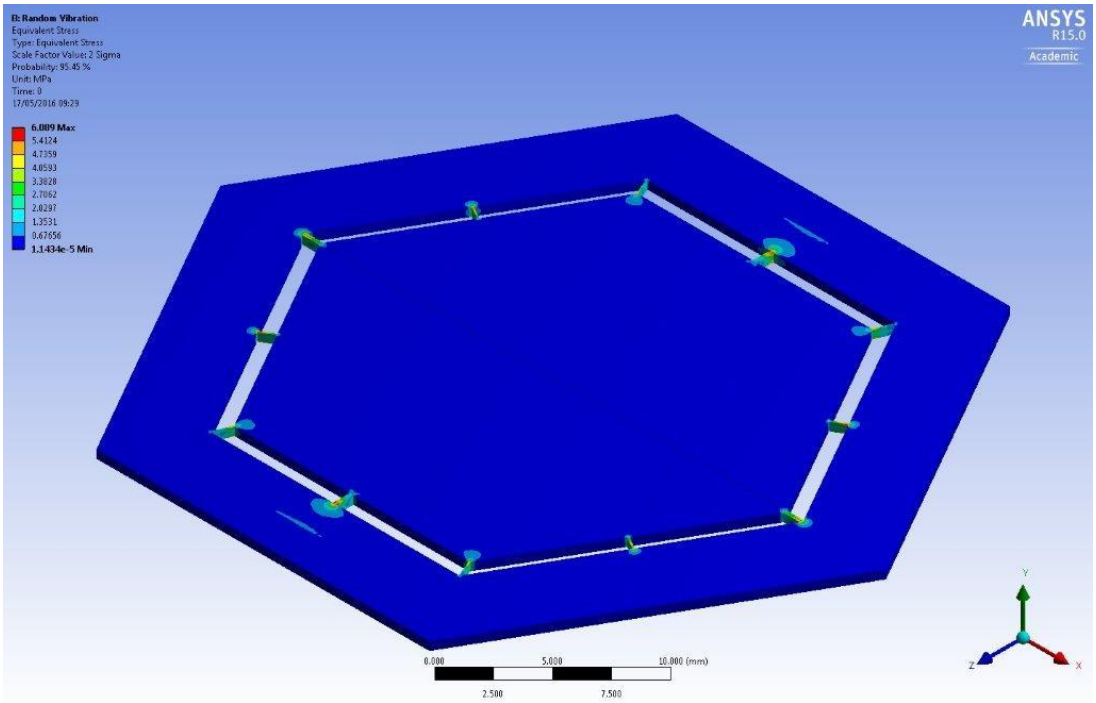

Figure 4.11: random vibration analysis: STRESS

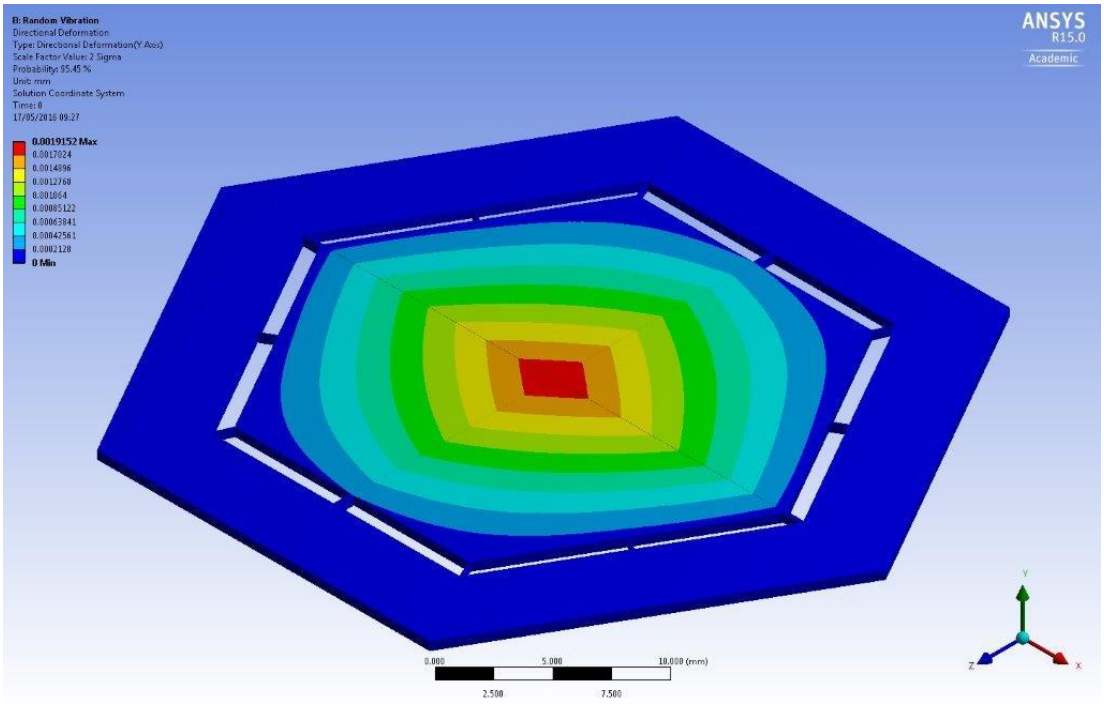

Figure 4.12: random vibration analysis: DISPLACEMENT

4.2. Test Structures

In order to evaluate some of the most important parameters, prior to the DM fabrication, some test structures have been set up. These are used mainly to validate the simulations conduced.

The most critical point is that regarding the thermal conductance of the silicon. Since we based our simulations and, thus, the detector design, upon a third-party reference, double-checking and understanding the real thermal conductance can help us to improve bridges shape to obtain the strongest structure by selecting the best Silicon provider.

These test structures also were a chance to set the best recipe to cut the structure using our Deep Reactive Ion Etching (DRIE) machinery.

The heat power flowing through a truss can be described by a generic function $W(T_1, T_2)$:

$$P = W(T_1, T_2) \tag{4.3}$$

Our temperatures refer to the rim and the suspended pixel, since we want to measure the gradient over the bridge connecting them. We can rewrite our function using the average temperature $T = (T_1 + T_2)/2$ and the temperature difference between the rim and the pixel: $\Delta T = T_1 - T_2$. Hence $P = W(T, \Delta T)$, so we can consider W at fixed T and expand around ΔT=0:

$$P = W_T(\Delta T) = W_T(0) + \frac{dW_T(0)}{d\Delta T}\Delta T \tag{4.4}$$

$W_T(0)=0$ for physical reasons, while the linear term represent the thermal conductance G of a specific object:

$$G(T) = \frac{dW_T(0)}{d\Delta T} \tag{4.5}$$

We can then write:

$$P = G(T)\Delta T \tag{4.6}$$

For a solid beam, the expression G(T) can be easily written as:

$$G(T) = k(T)\frac{s}{l} \tag{4.7}$$

Where s and l represent respectively the cross section and the length of the beam, while k(T) is the material intrinsic thermal conductivity. Its value is dependent on two contributions: free charge by conduction electrons and lattice vibrations:

$$k = k_e + k_p \tag{4.8}$$

When dealing with low temperatures, we must consider that both contributions have the same behaviour of the specific heat [41]: the electronic component has a linear dependence on the temperature, while the lattice one follows a third-power rule with the temperature, so that we can we can re-write the proportionality law for our conductance as follows:

$$G(T) = AT + BT^3 \tag{4.9}$$

Where A and B account for the thermal conductivity contributions by free electrons and lattice vibrations respectively, together with the geometrical factors of our beams.

In our simulations, we assumed, based on references, that the lattice contribution is dominant, so the overall thermal conductance can be approximated by a T^3 expression. This is mostly true, especially at low temperatures. However, a linear T term (coming from electron coupling) may appear even at very low temperature, depending, for instance, on the doping concentration of the silicon bulk

Since our detector performances are strongly dependant from this parameter, we decided to make a selection of wafers to probe the effective contribution of thermal conductivity.

We conduced some tests on different silicon samples, from commercially available doped (1-20 Ωcm) to low intrinsic (5 kΩcm) and higher grade of purity (>10 kΩcm).

To test the effective thermal conductance, we used DM-like structures, so to have a benchmark of the effective conductance we have to expect on the final model.

4.2.1. Setup and Results

We set up a recipe to produce micromachined Silicon chips by digging 90 degrees walls over 500 µm thick Silicon crystals. To do so, we upgraded our DRIE to be able to process a Bosch recipe [52] [53], useful to process Silicon microstructures, in which passivation phases with C_4F_8 alternate etching phases with SF_6 gases.

Results are very good, since we obtained well-shaped profiles: you can see an example in Figure 4.13, where we show a profile cross-section of a test wafer cut with our recipe, down to 50 µm, with the typical “scallops” structures well visible, due to the alternate etching/passivating phases, and a wall profile with a good cut angle very close to 90 degrees. In Figure 4.14 we show a meander-like structure cut over a 500 µm thick Silicon wafer.

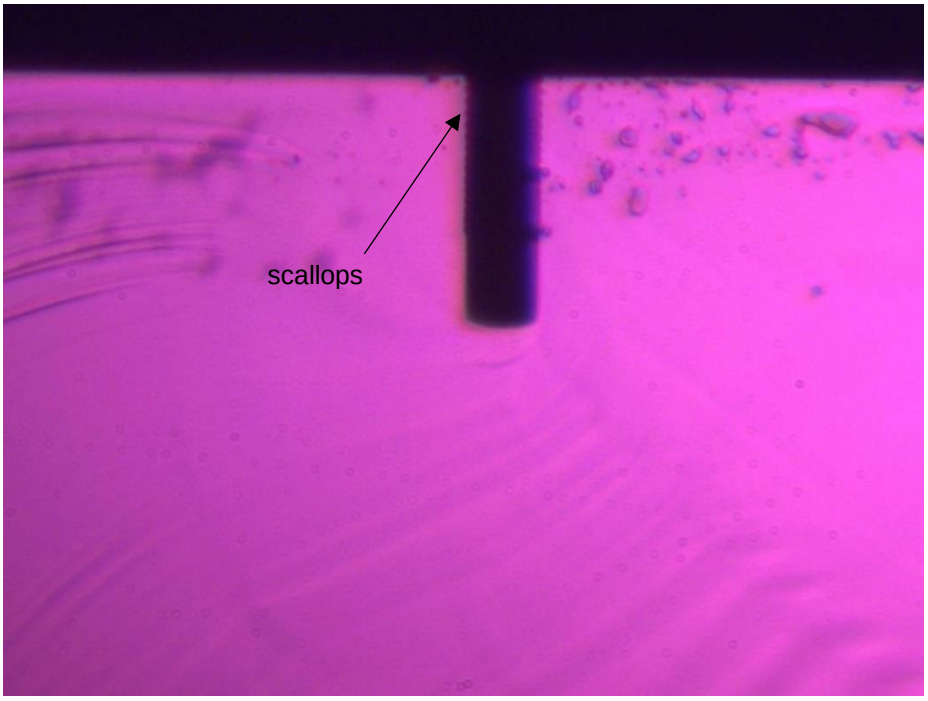

Figure 4.13: 20x magnification cross-sectional view of a sample wafer cut down to 50 µm. Scallops structures are well visible, as well as a very good steep wall dig.

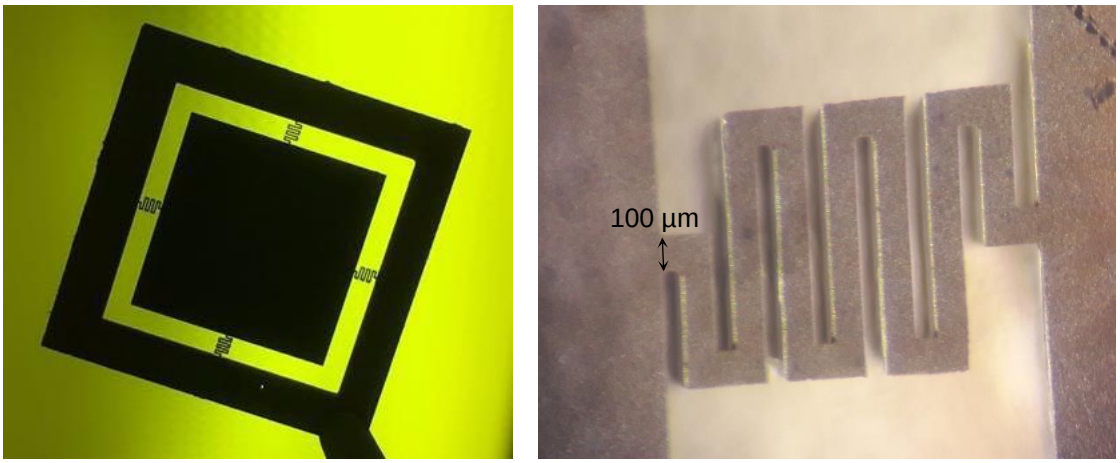

Figure 4.14: (LEFT) sample used to test our DRIE capabilities. (RIGHT) detail of one bridge.

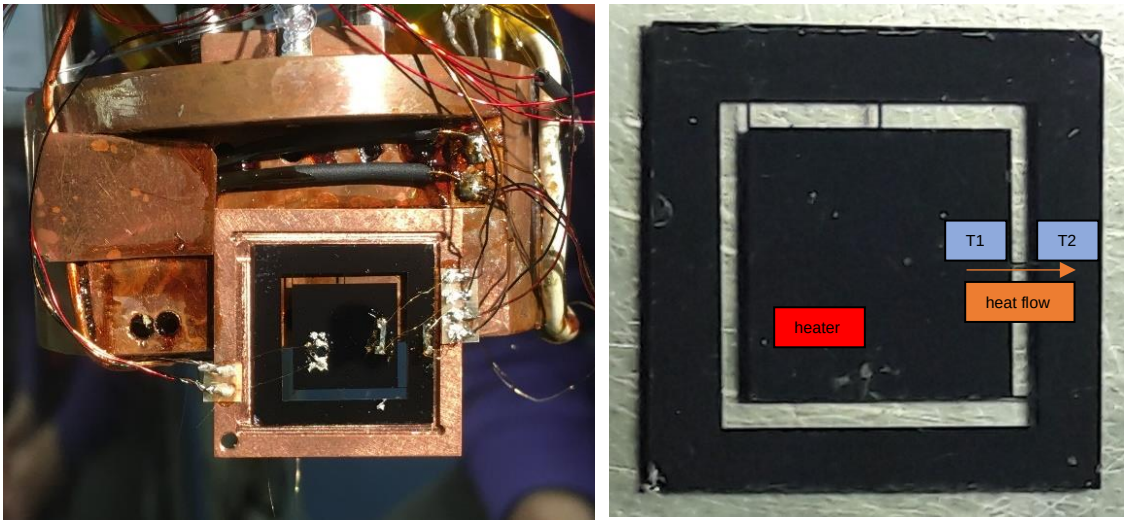

Figure 4.15: (LEFT) actual setup used to measure the thermal conductance for a DM-like structure. (RIGHT) setup scheme, where the heater dissipates power over the suspended chip, the heat flows through the 4 bridges and we measure the temperature drop along one of them (T1 and T2 are the GE thermometers).

Our samples were tested in our Kelvinox 25 dilution fridge. Figure 4.15 shows a picture of the sample mounted. We used a commercially available Pt meander structure grown over a small (4 mm^2) silicon chip to act as a heater. It was glued with GE Vanish 7031 glue onto the suspended pixel. Its resistance was measured to be on the order of hundreds of kΩ. Two Germanium thermometers were glued as well onto the test structure, one on the suspended pixel and one on the rim, each at the end of the same bridge, in order to measure the temperature drop across it. They were glued with GE Vanish 7031 glue as well. The thermal conductance of this glue is some order of magnitudes lower compared to that expected for our bridges, so it was not considered in our calculations [41]. The electrical connections were hand-made with the use of Au/Be wire bondings, 12 μm in diameter and 10 mm long, glued with EE149 EPO-TEK silver resin paste.

These bondings can contribute to the thermal conductance, allowing a fraction of the power to dissipate through them, instead of flowing along the bridges. For this reason, we made an evaluation of the thermal conductivity of a wire of a known length from the same stock, measured the resistance in a four wire configuration at liquid helium temperature, and found the theoretical thermal conductance through the empirical Wiedemann-Franz Law [54], which links the thermal

conductivity κ of a given metal to their resistivity (electrical conductance σ) with the following:

$$\frac{\kappa}{\sigma} = LT \qquad 4.10$$

Where $L = \frac{\kappa}{\sigma T} = \frac{\pi^2}{3}(\frac{k_B}{e})^2 = 2.44 \times 10^{-8}\ W\Omega K^{-2}$ is the Lorenz number [55].

The value found for our Au/Be wires was found to be negligible with respect to the bridges, due to their very small cross section.

The setup scheme is shown in Figure 4.16.

Thermometers are measured with a two wires setup, applying a common voltage of 0.5 mV and reading back both the voltage and their currents, through two Picoammeters Keithley 6485/6487. We use the cryostat temperature control to set the working point and the temperature feedback, and we recorded the two Germanium thermometers, at different T_0, applying a power dissipation onto the suspended pixel.

With a four wires setup we checked the heater's current and voltage drop while injecting power, ranging from 0 to ~1μW.

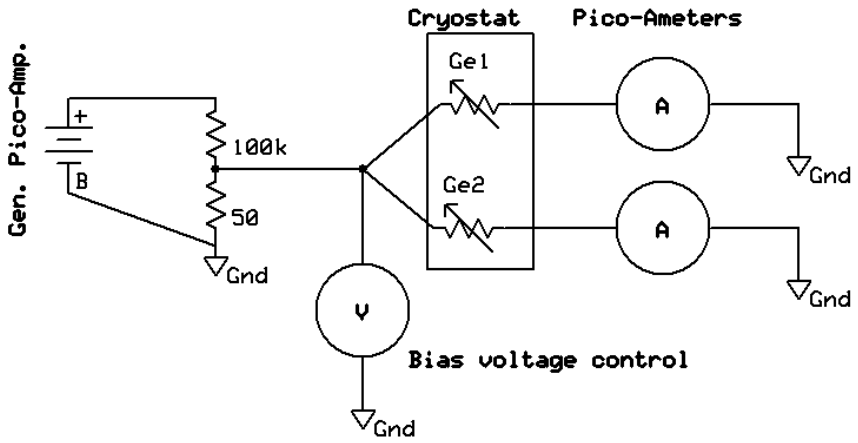

Figure 4.16: Setup scheme for the thermometers readout.

Thermometers calibration was obtained considering their resistance at 0 power applied, using the cryostat thermometer as reference.

For each cryostat temperature T_0, roughly from 450 mK down to 100 mK, we acquired the two R(P) curves related to the two Germanium thermometers. At every fixed T_0, we extrapolated the value for 0 power dissipated R(P=0). These represent the R(T) calibration curves of both thermometers. Then we used the relation [56]:

$$R(T) = R_0 e^{\sqrt{T_0/T}} \qquad 4.11$$

Where R_0 and T_0 are intrinsic parameters of each Germanium thermometer, summarized in Table 4.1 for the three samples we measured.

Sample	*Germanium*	$R_0\ [\Omega]$	$T_0\ [K]$
1	*GE1 (rim)*	*837.38 ± 2.02*	*20.89 ± 0.51*
	GE2 (pixel)	*538.39 ± 1.15*	*22.87 ± 0.53*
2	*GE1 (rim)*	*28.82 ± 0.67*	*6.94 ± 0.24*
	GE2 (pixel)	*9.08 ± 0.49*	*10.49 ± 0.35*
3	*GE1 (rim)*	*11.59 ± 0.56*	*8.24 ± 0.30*
	GE2 (pixel)	*8.34 ± 0.41*	*10.23 ± 0.33*

Table 4.1: Values for the intrinsic Germanium thermometers, obtained from the fit.

Once the calibration has been done, we acquired via a LabView routine every parameter in order to make a plot of P(ΔT) and, hence, of G(T).

Combining Equation 4.6 and Equation 4.7, and accounting for beams geometries and for the conductance measured for the Au/Be wires, we can find a plot for the thermal conductivity of our silicon samples. Using Equation 4.9 we find the thermal parameters of our silicon crystals, in order to evaluate the contribution of free electrons and lattice. Results are summarized in Table 4.2, where we obtained the two conductance parameters for our given geometries, and Table 4.3, where we calculated the resulting thermal conductance, rearranged for the

correct geometrical factors, accounting for 4 bridges. Figure 4.17 shows the total conductivity evaluated for three different silicon samples.

Sample	Resistivity	$A\ [\times 10^{-3}\ \frac{W}{K^2 \cdot m}]$	$B\ [\frac{W}{K^4 \cdot m}]$	$k@50\ mK\ [\frac{mW}{K \cdot m}]$
1	*1-20 Ωcm*	*391.5 ± 0.3*	*1.483 ± 0.003*	*19.76 ± 0.02*
2	*5 kΩcm*	*52.3 ± 0.9*	*2.095 ± 0.015*	*2.88 ± 0.05*
3	*>10 kΩcm*	*42.7 ± 0.4*	*0.829 ± 0.004*	*2.24 ± 0.02*

Table 4.2: Normalized fit parameters

Sample	Resistivity	$G@50\ mK\ [\frac{\mu W}{K}]$
1	*1-20 Ωcm*	*3.953 ± 0.002*
2	*5 kΩcm*	*0.576 ± 0.005*
3	*>10 kΩcm*	*0.448 ± 0.003*

Table 4.3: DM thermal conductance extrapolated at 50 mK

Sample	Resistivity	AT [%]	BT^3 [%]
1	*1-20 Ωcm*	*99.06*	*0.94*
2	*5 kΩcm*	*90.90*	*9.10*
3	*>10 kΩcm*	*95.37*	*4.63*

Table 4.4: Weight of the two terms in the total conductance @ 50 mK

As it can be seen in Table 4.4, the free electrons term is unexpectedly leading the overall thermal conductance, even at high sample purity levels.

Thus, that the overall thermal conductance of our detector will be slightly different from that expected.

Moreover, if the free electrons contribution is strong, the heat capacitance is also affected. Since, in the end, we are interested in the C/G ratio, the two terms could somehow compensate, leading to a correct detector response.

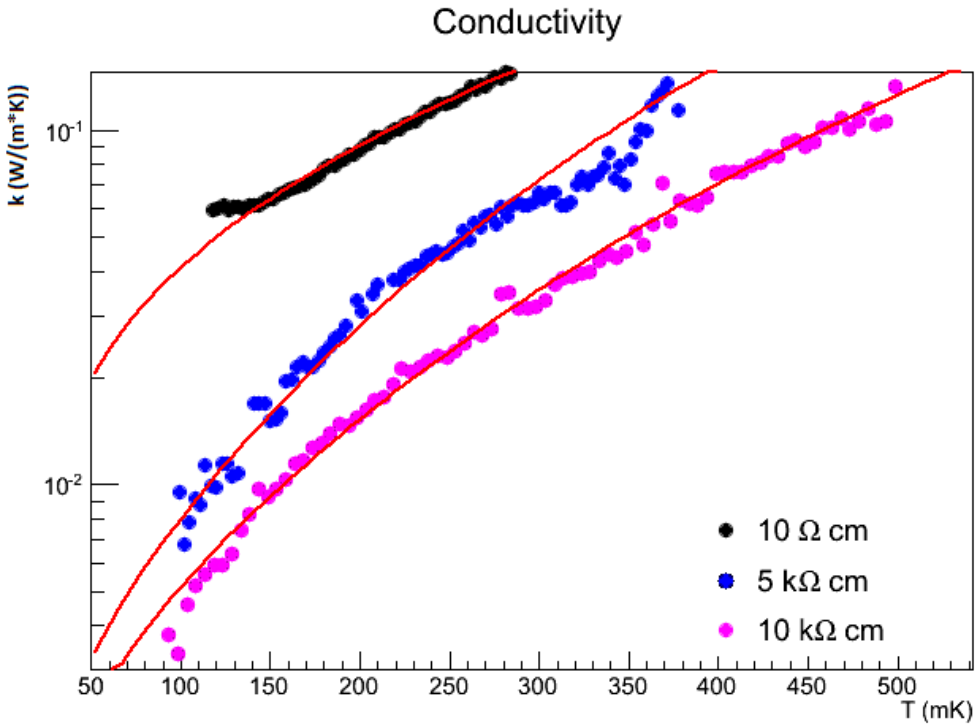

Figure 4.17: total thermal conductivity measured for our three silicon samples.

4.2.2. SIMS analysis

A side activity related to the study of the test structures concerns the analysis of the Silicon wafers we used to produce them.

High resistive Silicon does not mean high purity.

When a wafer contains an equal amount of donors and acceptors, it is called *"compensated"*, since the presence of donors and acceptors in a semiconductor causes the electrons given off by the donor to fall into the acceptor state which ionizes the acceptor without yielding a free electron or hole. In this situation we may have a high resistive Silicon specimen, which is all but pure.

While at room temperature this may not be a problem, when working at low temperature, the presence of both donors and acceptors plays a role.

Having a high purity wafer is, of course, more expensive, since we have to pay very high attention to every ppm or ppb of dopants.

We opened a contract with the facility *Fondazione Bruno Kessler* (FBK) in Trento, to have a complete analysis of some of the specimens we used for our measures.

They mainly carried a SIMS analysis. The SIMS analysis, whose acronym stands for Secondary-Ion Mass Spectrometry, is a technique used to analyse the composition of a solid surface or thin film by sputtering it with a focused ion beam of primary ions, usually noble gases ($^{40}Ar^+$, Xe^+), but also $^{16}O^-$, $^{16}O_2^+$, $^{16}O_2^-$, and even $^{133}Cs^+$. The sputtered product, which is formed by ejected secondary ions, is then analysed by a mass spectrometer.

Although it is mostly a qualitative analysis, it is possible to calculate the quantity of a given ion, if some calibration specimens are available for reference. This way, the SIMS is the most sensitive surface analysis technique, able to detect impurities as ppm or ppb [57]. Figure 4.18 shows a sketch of its working principle.

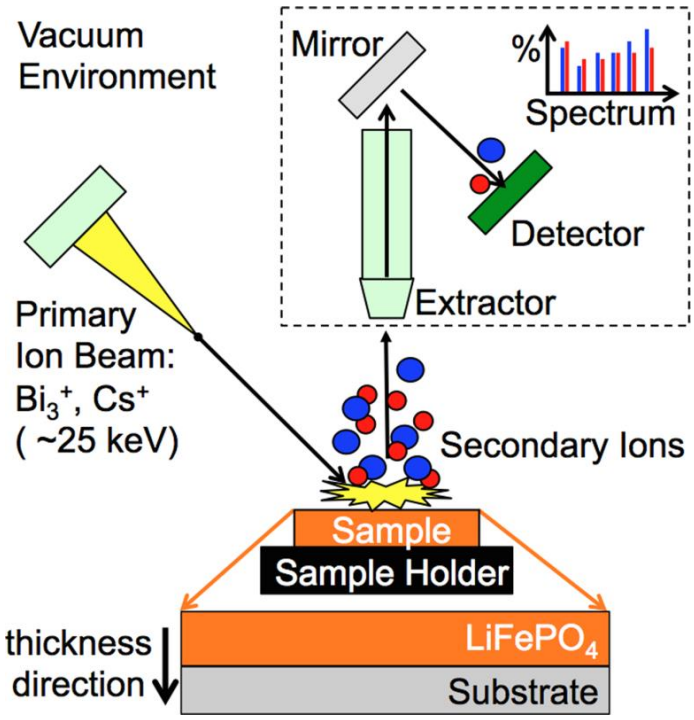

Figure 4.18: Working principle of a SIMS apparatus.

In FBK they used a CAMECA SC-Ultra to perform the SIMS analysis, using Cs and O as primary ion source. They looked for the following specimen: ^{14}N, ^{30}Si,

^{31}P, ^{7}Li, ^{11}B, ^{27}Al, ^{40}Ca, ^{64}Zn, in a reference matrix of ^{30}Si. The total area analysed was $50 \div 75$ µm in diameter, for an overall 1 µm depth. Results are shown in Figure 4.19, Figure 4.20, and Figure 4.21. Table 4.5 visually summarizes the total amount of specimens found in each sample. Principal atoms used as dopants are highlighted in red. As we can see, for the first sample, the number of B atoms is very high, suggesting it is a P-type Silicon wafer, which is actually what it's stated by the production company, and so it could be considered as a double-check on the reliability of the analysis. In the second sample, whose resistivity is declared to be 5 kΩcm, the total amount of B and P atoms is the same, suggesting it is a compensated Silicon wafer. The latest sample, which should be the purest one, shows a lower level of B atoms, but an excess of P, suggesting it is more likely to be an N-type Silicon wafer.

The three specimens analysed have a high concentration of dopant, which could be the cause of the dominant free electrons contribution to the thermal conductance.

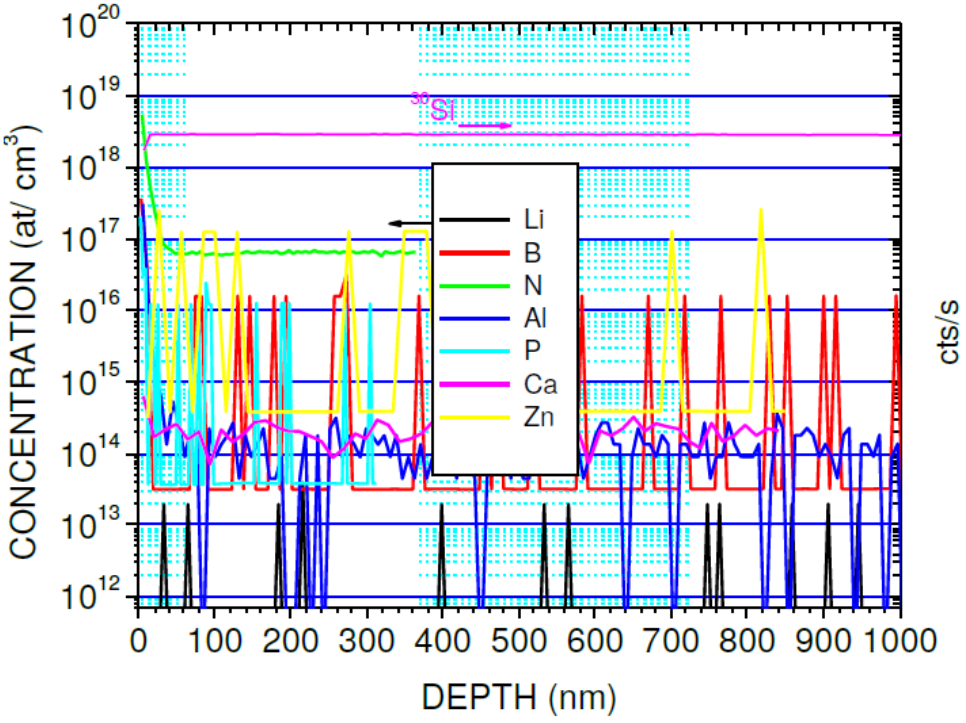

Figure 4.19: Specimen 328 (our reference sample 1): 1-20 Ωcm. SIMS analysis.

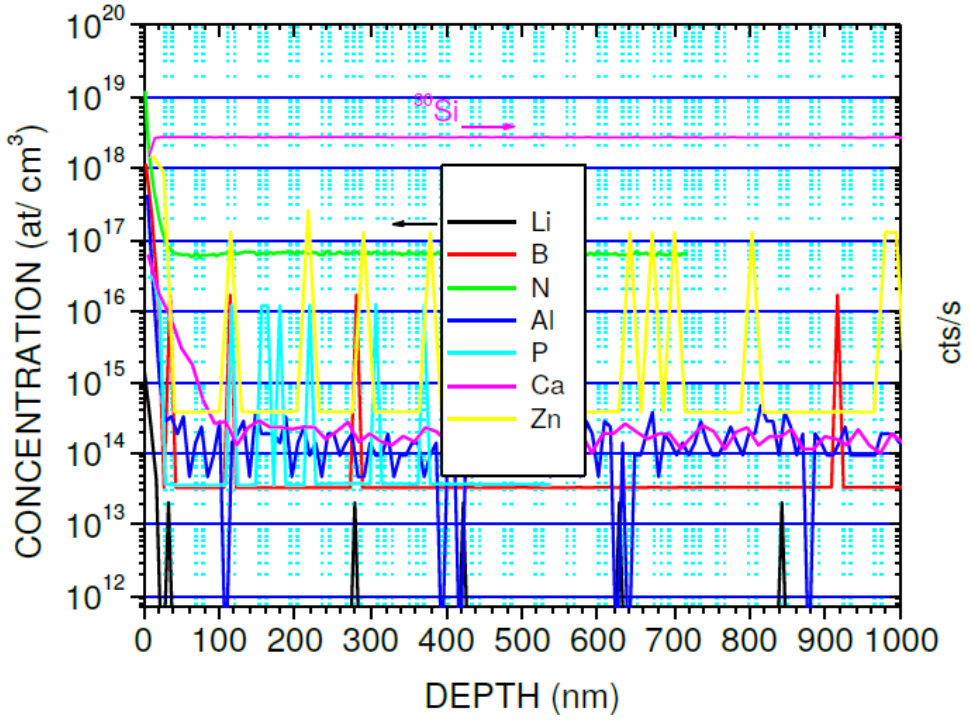

Figure 4.20: Specimen 329 (our reference sample 2): 5 kΩcm. SIMS analysis.

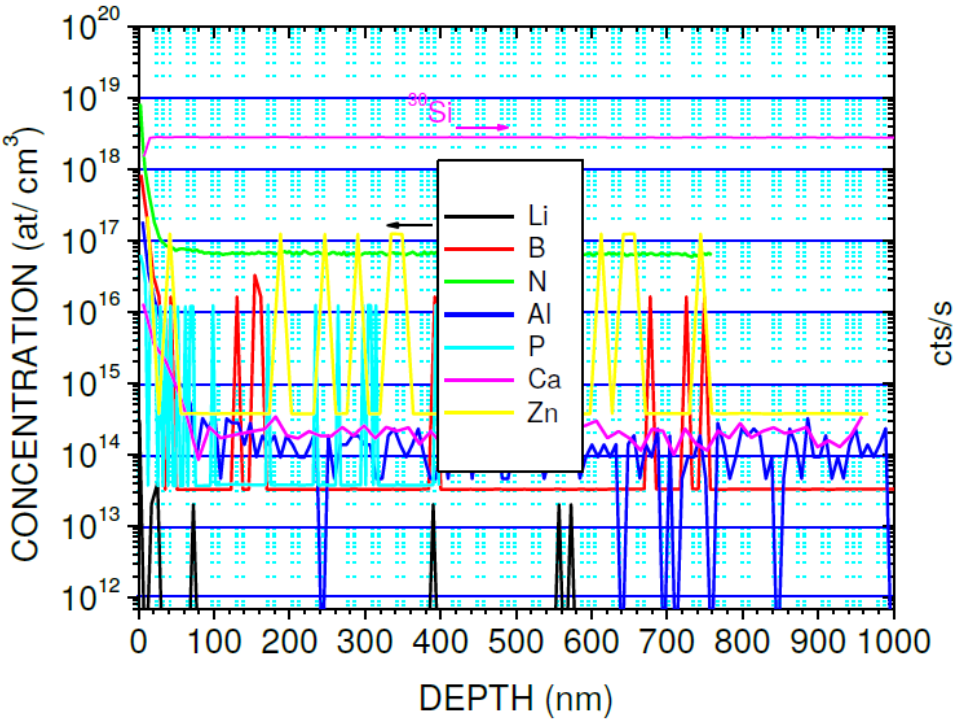

Figure 4.21: Specimen 330 (our reference sample 3): >10 kΩcm. SIMS analysis.

Sample (FBK)	Sample (our ref.)	Resistivity	SIMS [atoms/cm^3]
328	1	1-20 Ωcm	Li = 2 E12 B = 2.3 E15 N = 6.5 E16 Al = 1.3 E14 P = 1.4 E15 Ca = 1.9E14 Zn = 3.0E16
329	2	5 kΩcm	Li = 7 E11 B = 7.0 E14 N = 6.4 E16 Al = 1.5 E14 P = 7 E14 Ca = 1.7E14 Zn = 2.4E16
330	3	>10 kΩcm	Li = 9 E11 B = 8.2 E14 N = 6.4 E16 Al = 1.3 E14 P = 1.4 E15 Ca = 2.0E14 Zn = 2.6E16

Table 4.5: Main dopant concentration found for the SIMS analysis of our Silicon samples.

Conclusions

The study for a cryogenic Anticoincidence detector begun more than 10 years ago, when the project foreseen to send a small detector in orbit to probe its skills to do some Astrophysics. As time passed by, more interest arose in making this mission even bigger and more technologically challenging, in order to obtain better results and do more Astrophysics.

It has been exciting to see, in 2014/2015, that the mission was finally adopted and confirmed: from then on, the mere work on R&D would have been transformed in something much more result-oriented. We were a growing community, and we finally had a focus.

Since then, the development of the best detector has been a very exciting challenge. The results we found on the many prototypes we manufactured, also made us confident that the right direction was taken.

AC-S1 opened the way to this kind of research. We found a lot of information on phonon-mediated TESs. Further developments were necessary to reach a good trade-off to obtain large area detectors based on this technology. Every step we made helped us improving our knowledge and the efficiency of the detector. AC-S5 was another leap forward, since we found more information related to the effectiveness of Iridium multi-TES detectors. AC-S7 and AC-S8 were AC-S5 natural evolution, since we put even more Iridium TESs, a strategy which allowed use to scale for even bigger detectors.

The understandings from AC-S1 to AC-S8 made us more confident on the behaviour of Iridium TESs grown over Silicon absorbers, a field where few others made researches.

With every detector we manufactured, we made a step forward, enhancing both our knowledge and our method on producing, analysing and improving our detectors chain production.

The Demonstration Model will be the final step, the dividing line between what was pure R&D and what will be the first anticoincidence detector based on transition-edge sensor technology to be launched on a space mission. Although ASTRO-H has been the first mission adopting TES technology for X-Ray astrophysics, it did not make use of an active anticoincidence of this level (see [58] [59]).

We payed special care on every aspect, but we have to improve even more: too many parameters need to be controlled. We have seen that the wafer quality is not easily controllable. However, having a purity different from what we expected to work with, could be compensated giving way to the right performances we want to have.

The fabrication of the Demonstration Model itself will be the test for those parameters we cannot control, and also for those we have theorized and simulated for long time. The results of its analysis will highlight what it will be necessary to implement on the Flight Model, taking a major advance in the final object.

During my PhD I’ve been an active part of the CryoAC manufacturing process: from the analysis on previous samples, to the study, design and development of new prototypes.

I brought the design and specifics of the detector to a more mature level, allowing the collaboration to reach an adequate level of readiness.

As the end of the phase A will approach, our knowledge on the detector will be complete, and we will be ready to test the final detector together with the main X-Ray array. This will be very important, since at that time most of the work will be done, and only an implementation on the final focal plane assembly will be necessary after.

The Demonstration Model represents the state-of-art of our knowledge regarding our application of TES technology. We are eager to test it to probe its capabilities.

Yet, we are inspired by our goal, remembering that our object is going to fly for the first time ever on a space mission.

Ringraziamenti

È doveroso aprire questo capitolo ringraziando il prof. Flavio Gatti. Quando ho messo piede in L103, cercando una tesi di laurea, e l'ho incontrato con la sua felpa comprata direttamente da NASA GSFC, sapevo che quello sarebbe stato il mio laboratorio. Lui mi ha reso possibile arrivare fin dove sono ora, negli ultimi cinque anni, aprendomi ad un mondo di ricerca meraviglioso che mi ha entusiasmato. Mi ha insegnato tanto. Non solo di fisica.

Ringrazio di cuore tutto il team di L103. Ringrazio Daniela e le pizze in sua compagnia in attesa di un vuoto in camera. La ringrazio per avermi insegnato come lavorare in camera pulita senza sbattere la testa per la disperazione, con pazienza ed entusiasmo. Entusiasmo che a Michele un po' manca, lo ammetto, ma che compensa con un sacco di altre qualità: dedizione, correttezza, capacità, curiosità. Lo ringrazio per avermi affiancato e visto crescere da vicino, senza mai abbandonarmi quando uno sviluppo o una transizione non venivano.

Ringrazio particolarmente Matteo e Giulio per avermi reso meno pesanti le ore a smontare un cannone elettronico, e non solo!

Ringrazio Elisa, Valentina, Giovanni, Daniele, compagni di sventura, risate, chiacchiere e caffè.

Ringrazio Adriano, Luigi e Fabio, colonne del laboratorio, e da cui ho appreso molto.

Siete per me tutti amici prima che colleghi.

Dario

Genova, 26/03/2018

References

[1] R. Giacconi, H. Gursky, F. R. Paolini and B. B. Rossi, “Evidence for X-rays from sources outside the solar system,” *Phys. Rev. Lett.,* vol. 9, no. 11, pp. 439-443, 1962.

[2] HEASARC, NASA, [Online]. Available: https://heasarc.gsfc.nasa.gov/docs/einstein/heao2.html.

[3] Observatory, Chandra X-Ray, [Online]. Available: http://cxc.harvard.edu/proposer/POG/html/chap6.html#tth_chAp6.

[4] R. Giacconi, “Nobel Lecture: The dawn of x-ray astronomy,” *REVIEWS OF MODERN PHYSICS,* vol. 75, 2003.

[5] K. Nandra, X. Barcons, J.-W. den Herder, M. Watson, D. Barret, A. Fabian and L. Piro, “ATHENA The Advanced Telescope for High Energy Astrophysics, A mission addressing The Hot and Energetic Universe science theme,” 2014. [Online]. Available: http://userpages.irap.omp.eu/~dbarret/ATHENA/The_Athena_Mission_Proposal.pdf.

[6] K. Nandra, “The Hot and Energetic Universe: A White Paper presenting the science theme motivating the Athena+ mission, www.the-athena-x-ray-observatory.eu,” *arXiv 1306.2307,* 2013.

[7] J. Kaastra, A. Finoguenov, F. Nicastro and al., “The Hot and Energetic Universe: the Missing Baryons and the Warm-Hot Intergalactic Medium,” *arXiv 1306.2324,* 2013.

[8] J. H. Croston, J. S. Sanders and al., “An Athena+ supporting paper: AGN feedback in galaxy clusters,” *2013arXiv1306.2323.*

[9] J. Magorrian and al., “The Demography of Massive Dark Objects in Galaxy Centres,” *arXiv:astro-ph/9708072, Astron.J.,* vol. 115, no. 2285, 1998.

[10] T. Di Matteo and al., “Energy input from quasars regulates the growth and activity of black holes and their host galaxies,” *doi:10.1038/nature03335, Nature,* vol. 433, pp. 604-607, 2005.

[11] A. Georgakakis, F. Carrera and al., “Understanding the build-up of supermassive black holes and galaxies at the heyday of the Universe,” *www.the-athena-x-ray-observatory.eu, (arXiv 13062328),* 2013.

[12] T. Takahashi and al., “The ASTRO-H Mission,” *SPIE, 7732, pp. 77320Z-77320Z-18,* 2010.

[13] Hitomi Collaboration, “Hitomi Constraints on the 3.5 keV Line in the Perseus Galaxy Cluster,” *ApJ Letters,* 2017.

[14] Hitomi Collaboration, “The Quiescent Intracluster Medium in the Core of the Perseus Cluster,” *Nature,* vol. 535, pp. 117-121, 2016.

[15] M. Bavdaz and al., “The ATHENA Optics Development,” *Proc. SPIE 9905 990527, doi 10.1117/12.2233037,* 2016.

[16] N. Meidinger and al., “The Wide Field Imager Instrument for Athena,” *arXiv:1702.01079,* 2016.

[17] D. Barret, T. L. Trong, J. W. den Herder, L. Piro and al., “The Athena X-Ray Integral Field Unit (X-IFU),” *Proc. SPIE 9905 99052F, doi 10.1117/12.2232432,* 2016.

[18] U. Nagel and al., “Proximity Effect in Iridium/Gold Bilayers,” *Journal of Applied Physics,* vol. 76, pp. 42-46, 1994.

[19] NIST. [Online]. Available: http://physics.nist.gov/cgi-bin/Xcom/xcom3_1.

[20] D. H. Andrews, *Rev. Sci. Instr.,* vol. 13, pp. 281-292, 1942.

[21] D. H. Andrews, *Phys. Rev.,* vol. 76, pp. 154-155, 1949.

[22] J. Clarke and A. Braginski, “The SQUID handbook: Volume 1: Fundamentals and Technology of SQUIDs and SQUID systems.,” 2004.

[23] R. Fagaly, *Rev. Sci. Instr.,* vol. 77, 2006.

[24] K. D. Irwin, *Applied Physics Letters,* vol. 66, pp. 1998-2000, 1996.

[25] K. D. Irwins and al., *Applied Physics Letters,* vol. 69, pp. 1945-1947, 1996.

[26] K. D. Irwin and G. C. Hilton, “Transition-Edge Sensors,” in *Cryogenic Particle Detection*, Springer-Verlag Berlin Heidelberg 2005, 2005, pp. 63-149.

[27] K. D. Irwin and G. C. Hilton, “An Application of Electrothermal Feedback for High Resolution Cryogenic,” *Applied Physics Letters,* vol. 66, p. 1998, 1995.

[28] C. Enss, Cryogenic Particle Detection, Springer, 2005.

[29] J. N. Ullom and al., *Applied Physics Letters,* vol. 87, no. 194103, 2005.

[30] E. V. Bezuglyi and V. Vinokur, “Heat Transport in Proximity Structures,” *Phys. Rev. Letters,* 2003.

[31] F. Gatti and al., “Ir TES Electron-Phonon Thermal Conductance and Single Photon Detection,” *Journal of Low Temperature Physics,* 2008.

[32] F. Pröbst and al., “Model for Cryogenic Particle Detectors with Superconducting Phase Transition Thermometers,” *Journal of Low Temperature Physics,* vol. 69, p. 100, 1995.

[33] S. Lotti and al., “Estimate of the Impact of Background Particles on the X-Ray Microcalorimeter Spectrometer on IXO,” *Nuclear Instruments and Methods,* vol. 686, 2012.

[34] S. Lotti and al., “In-Orbit Background of X-Ray Microcalorimeters and its Effects on Observations,” *Astronomy and Astrophysics,* vol. A54, no. arXiv:1410.3373, p. 569, 2014.

[35] S. Lotti and al., “An Efficient Method for Reducing the Background of Microcalorimeters Applied to ATHENA-XMS,” *Proc. of SPIE 8443 84435H, doi 10.1117/12.925443,* 2012.

[36] G. W. Fraser, “X-Ray Detectors in Astronomy,” *Cambridge Astrophysics Series,* 1989.

[37] C. Macculi and al., “The Cryogenic Anticoincidence Detector for ATHENA X-IFU: a Program Overview,” *Proc. SPIE 9905 99052K, doi 10.1117/12.2231298,* 2016.

[38] C. Macculi and al., “The TES-Based Cryogenic Ancticoincicidence Detector for IXO: First Results from Large Area Prototypes,” *Proc. of SPIE Vol 7732 773223Y-1,* 2010.

[39] C. Macculi and al., “The Cryogenic Anticoincidence Detector for ATHENA-XMS,” *J. Low Temp. Phys,* vol. 167, pp. 783-794, 2012.

[40] M. Pyle and al., “Quasiparticle Propagation in Aluminium Fins and Tungsten TES,” *Nuclear Instruments and Methods,* vol. 559, 2006.

[41] O. V. Lounasmaa, Experimental Principles and Methods Below 1K, Academic Press, 1974.

[42] M. E. Msall and J. P. Wolfe, “Ballistic phonon production in photoexcited Ge, GaAs, and Si,” *Phys. Rev. B,* vol. 65, 2002.

[43] E. Gatti, M. Sampietro and P. F. Manfredi, “Optimum Filters for Detector Charge Measurements in Presence of 1/f Noise,” *Nucl. Instr. and Methods,* vol. A287, pp. 513-520, 1990.

[44] E. Gatti, M. Sampietro, P. F. Manfredi and V. Speziali, “Suboptimal Filtering of 1/f Noise in Detector Charge Measurements,” *Nucl. Instr. and Methods,* vol. A297, pp. 467-478, 1990.

[45] M. D'Andrea, A. Argan, D. Corsini, C. Macculi, L. Piro, M. Biasotti, S. Lotti, F. Gatti and G. Torrioli, “The Cryogenic Anti-Coincidence detector for ATHENA X-IFU: Pulse Analysis of the AC-S7 Single Pixel Prototype,” *Proc. SPIE 9905 99055x, doi: 10.1117/12.2231412,* 2016.

[46] M. Galeazzi and al., “Iridium thin films deposited via pulsed laser deposition,” *Nuclear Inst. and Methods in Physics Research, A,* vol. 520, no. 1-3, pp. 293-295, 2004.

[47] J. A. Chervenak and al., “Fabrication of Microstripline Wiring for Large Format Transition Edge Sensor Arrays,” *J. Low Temp. Phys.,* vol. 167, pp. 547-553, 2012.

[48] T. Sota, K. Suzuki and D. Fortied, “Low-temperature thermal conductivity of heavily doped p-type semiconductors,” *J. Phys. C: Solid State Phys.,* vol. 17, pp. 5935-5944, 1984.

[49] K. E. Petersen, “Silicon as a Mechanical Material,” *Proceedings of the IEEE,* vol. 70, no. 5, pp. 420-456, 1982.

[50] ATHENA on ESA website, “http://sci.esa.int/cosmic-vision/54517-athena/,” [Online].

[51] D. Corsini and al., “The mechanical and EM simulations of the CryoAC for the ATHENA X-IFU,” *Proc. SPIE 9905 99055y, doi:10.1117/12.2232499,* 2016.

[52] Lärmer, F.; Schilp, A.; Robert Bosch GmbH,, “Method of Anisotropically Etching Silicon,” *US-Patent No. 5501893.*

[53] F. Lärmer and A. Schilp, “Bosch Deep Silicon Etching: Improving Uniformity and Etch Rate for Advanced MEMS Applications,” *Twelfth IEEE International Conference on Micro Electro Mechanical Systems, MEMS '99,* 1999.

[54] J. William and H. M. Norman, Theoretical Solid State Physics, Courier Dover Publications, 1985.

[55] C. Kittel, Introduction to Solid State Physics, John Wiley and Sons, 2005.

[56] G. K. White and P. J. Meeson, Experimental Techniques in Low-Temperature Physics, 4th Edition, Oxford Science Pulications, 2002.

[57] A. Benninghoven, F. G. Rüdenauer and H. W. Werner, Secondary Ion Mass Spectrometry: Basic Concepts, Instrumental Aspects, Applications, and Trends, New York: Wiley, 1987.

[58] C. A. Kilbourne and al., “The design, implementation, and performance of the Astro-H SXS calorimeter array and anti-coincidence detector,” 2017. [Online]. Available: https://ntrs.nasa.gov/search.jsp?R=20160008077 2017-10-31T09:11:53+00:00Z.

[59] R. L. Kelley and al., “The Suzaku High Resolution X-Ray Spectrometer,” *Publ. Astron. Soc. Japan,* no. 59, p. S77–S112, 2007.